Pre-print submitted version

Highly efficient thermally co-evaporated perovskite solar cells and mini-modules

Jia Li, [a] Hao Wang, [a] Xin Yu Chin, [a] Herlina Arianita Dewi, [a] Kurt Vergeer, [a], Teck Wee Goh, [b] Jia Wei Melvin Lim,[a, b] Jia Haur Lew, [a] Kian Ping Loh [c] Cesare Soci,[b] Tze Chien Sum, [b] Henk Bolink, [d] Nripan Mathews, [a,e*] Subodh Mhaisalkar, [ae*] Annalisa Bruno [a*]

[a.] *Energy Research Institute @ NTU (ERI@N), Nanyang Technological University, Singapore 637553.*

[b.] *Division of Physics and Applied Physics, School of Physical and Mathematical Sciences, Nanyang Technological University, 21 Nanyang Link, 637371, Singapore*

[c.] *Department of Chemistry, National University of Singapore, 3 Science Drive, Singapore 117543*

[d.] *Instituto de Ciencia Molecular, Universidad de Valencia, C/J. Beltra´n 2, 46980, Valencia, Spain.*

[e.] *School of Materials Science & Engineering, Nanyang Technological University, Singapore, 639798.*

Corresponding authors: annalisa@ntu.edu.sg, nripan@edu.sg, subodh@ntu.edu.sg

* Lead Contact: annalisa@ntu.edu.sg

Summary

The rapid improvement in perovskite solar cells' (PSCs) power conversion efficiency (PCE) has prompted the interest to adapt the perovskite technology in the production lines. Capitalizing on existing industrial processing methods will facilitate technology transfer from lab-scale research into mass production, thereby accelerating commercialization. In this work, we prove the scalability of high quality thermally co-evaporated $MAPbI_3$ active layers in perovskite solar cells and mini-modules, being able to guarantee minimal PCE losses, when PSCs are scaled up to larger active areas. With a combined strategy of active layer engineering based on deposition optimization, effective surface and interfacial treatments and light-dispersion minimization, we demonstrate PSCs (active area of 0.16 cm^2) and mini-modules (active area 21 cm^2) achieving record PCEs of 20.28% and 18.13% respectively. The un-encapsulated PSCs were

able to retain ~ 90% of their initial PCE under continuous illumination at 1 sun (AM 1.5G), without active sample cooling, for over 100 h. Looking towards both tandem applications and building integrated photovoltaic (BIPV), we have also demonstrated thermally co-evaporated perovskite semi-transparent modules and semi-transparent PSCs. Coloured small-area PSCs showed consistent PCEs around 16% for a set of colors spanning the whole visible range. Our work demonstrates the compatibility of perovskite technology with existing industrial processes and its potential for the next-generation photovoltaics on the market.

Introduction

Undertaking the substantial electricity de-carbonization compelled by the Paris Climate Agreement by 2020 [1], while meeting the ever-increasing energy demands, requires disruptive developments of renewable energy. Given the enormous solar irradiance received on the Earth, photovoltaic is one of the most appealing options to meet the immediate needs at a similar competitive cost as fossil fuels-generated electricity.

In this regard, metal-halide perovskites have recently emerged as one of the most promising low cost photovoltaic [2-5] and optoelectronic [6-9] technology. Indeed, their excellent optoelectronic properties, such as long carrier diffusion length, low defect densities, and high carrier mobilities [10-14] and their versatility in producing high-quality thin films[15-17], have been the key aspects to drive the development of this technology. Since the advent of the first perovskite solar cells (PSCs) in 2009,[18] their power conversion efficiency (PCE) has reached 25.2%.[19] In addition, the unique band-gap tunability of perovskite absorber has been explored for engineering semi-transparent PSCs (ST-PSCs) with suitable optical bandgap to complement the absorption of Si solar cells for high-efficiency tandem solar cells.[20-27] Moreover, highly efficient ST-PSCs have shown great potentials as building integrated photovoltaic (BIPV) architectonic elements to improve buildings and city landscapes aesthetics while harvesting solar energy.[28,29]

On the other hand, the best-performing PSCs are yielded by the favored lab-scale solution-processed techniques on small scale (~0.1 cm^2) devices.[30-34] Most of the advancements in those PSCs architectures are unfortunately not transferable to the fabrication of perovskite solar modules (PSMs) which are instead necessary for field-applications and to reduce generated power production cost.

Indeed, when PSCs are scaled up to larger active areas, the most significant PCE losses are due to the increased series resistance, caused by the limited sheet conductivity of most transparent-conductive oxides as well as by the non-uniformity of the active layer over larger areas. The high resistivity can partially be compensated/recovered by connecting thin strips of PSCs, in series connection, into PSMs. The serial connection is enabled by multiple scribing on the PSMs, resulting in optical losses due to the dead aperture area, mechanical and laser scribing methods have been commonly used to minimize the inactive areas.[35,36] Meanwhile, most of the research efforts on PSMs have been poured into engineering large-area perovskite thin film with low defect

density, large crystal grain, and low surface roughness. In this regard, blade-coating[37-41] spray coating,[42] slot die coating,[43,44] spin-coating with anti-solvent,[45-55] one-step,[56-59] two-steps,[60-62] and hot casting[63] methods have been successfully implemented to deposit high quality, large-area perovskite thin films. Recently, Qi and co-workers developed a hybrid chemical vapor deposition and cation exchange (HCVD-CE)[64,65] method combined with spin-coating for depositing large area perovskite thin films. A solvent- and vacuum-free route, where amine complex precursors are rapidly converted to perovskite phase with a simple pressure application step, have been demonstrated to fabricate PSM with an active area of 36.1 cm^2 achieving a certified PCEs of 12.1%.[66] Nevertheless, the development of high-quality transporting/interfacial layers for PSMs is also equally important to ensure efficient carrier extraction from the active perovskite layer.[39,46-48,51,53,54,59,61,67] Huang et. al. also demonstrated efficient PSM realized by surfactant-assisted blade-coating achieving 15.3% over an active area of 33 cm^2. [68] Di Carlo and co-workers employed 2D materials as charge transporting/extraction layers, demonstrating PCEs of 13.4% on PSMs with an active area of 108 cm^2.[47,67] Besides, proper interfacial treatments also enabled depositing high-quality poly(3-hexyl) thiophene (by bar-coating) and SnO_2 nanoparticles (by electrostatic self-assembly spin-coating) as transporting layers, delivering PSM with record PCEs of 17.1%(stabilized 16.1%) [59] and 15.3%[46] for PSMs with active area of ~25 cm^2. Moreover, Grancini et al[69] recently demonstrated 10x10 cm^2 PSMs (active area ~ 47.6 cm^2) fabricated by a fully printable industrial-scale process. These PSMs exhibit 11.2% efficiency and stable for more than 10,000 hours, an important milestone towards the commercialization of perovskite photovoltaic. **Table S1** summarizes the high performances (PCE>10%) large areas PSCs and PSMs with active areas larger than 10 cm^2 fabricated with different perovskite compositions and deposition methods.

To accelerate the market-entry of perovskite technology, the processing of the active materials should be performed with an established and widely adopted coating technique in the semiconductor industry. The vacuum-based physical deposition method, as exemplified by the commercialization of the fully evaporated organic light-emitting diodes for display and lighting applications, is an industrial scale method that allows the sequential deposition of functional materials to form a multi-layers' architecture. The real challenge for producing high-quality vacuum-deposited perovskite thin films arises from the complicating multiple sources co-deposition processes, where the deposition rates of every precursor must be precisely tuned to get a stoichiometric composition for the formation of perovskite. However, the method is still to offer multiple advantages over the solution-processed counterparts as the higher purity of the sublimed materials a precise control of the deposited film thickness and the last but not least the elimination of toxic solvents for thin-film formation.

Previously, Snaith and co-workers were the first to demonstrate a 15.4% PSCs based on thermally evaporated perovskite active layers, achieved by co-evaporation of the organic and inorganic precursors.[70] With the prototypical methyl-ammonium (MA) lead iodide active layer, Bolink and co-workers demonstrated fully evaporated PSCs with efficiencies of 16.5% and 20.3% achieved for the p-i-n and n-i-p architecture (active area ~ 0.1 cm^2), respectively.[71] The same team has further demonstrated the versatility of the co-evaporation method, demonstrating of high performance mixed Cs, formamidinium (FA), and MA triple cations perovskite solar cells with efficiency over 16%.[72] Up to now, only hybrid deposition methods based on a combination of vacuum deposition of the inorganic components and solution/solvent vapor deposition of the organic precursors have been implemented to deposit large-area (>100 cm^2) perovskite thin films,[73]. The hybrid deposition methods have been also utilized to achieve a conformal coating of perovskite on a fully textured silicon surface enabling a monolithic 2-terminal perovskite/silicon tandem solar cell [21] and monolithic triple-junction perovskite/perovskite/silicon tandem solar cells.[74] Here we demonstrate highly efficient MAPbI$_3$ PSCs where the active perovskite layer was deposited by thermal co-evaporation. Our approach to improve the overall PSCs performances is based on a combined strategy of active layer engineering coupled with effective surface treatment, charge extraction enhancement and optical light-dispersion minimization. The best PSC architecture gives the highest PCE of 20.28% (active area ~ 0.16 cm^2), and no losses observed in open-circuit voltage and short-circuit current when the active areas have been scaled to 4 cm^2. The un-encapsulated PSCs also show a PCE stability ~90% under 1 sun (AM 1.5G) continuous illumination for over 100 hours. The optimised device architecture is transferable from lab-scale prototypes to large-area mini-modules, enabling the demonstration of PSMs with PCE > 18% and active area ~21 cm^2 representing the most efficient reported to the best of our knowledge. Finally, we show that the same architecture can directly be utilized in fabricating ST-PSCs and semi-transparent PSMs (ST-PSMs) with an active area efficiency of 16.8% and 11.2% achieved from active area of 0.16 cm^2 and 16 cm^2, respectively. For the first time we also demonstrate thermally evaporated coloured PSCs. Our work proves the scalability and versatility of thermal co-evaporation methods in realizing PSMs representing a critical step with industrial standard for the commercialization of perovskite technology.

Results and Discussion

Figure 1a shows the planar n-i-p architecture of the perovskite solar cell (PSC) structure implemented in this work. A MAPbI$_3$ film, deposited by thermal co-evaporation process of PbI$_2$ and CH$_3$NH$_3$I (MAI) as illustrated in the inset of **Figure 1a**, is used as absorbing layer. The details of the experimental conditions are provided in the experimental section. A planar architecture is the best device structure for evaporated perovskites as they cannot fully infiltrate into a mesoporous structure. PSCs architectures implemented in this work incorporated a fluorine doped tin oxide (FTO) coated glass as substrate and bottom electrode and either compact TiO$_2$ or SnO$_2$ films as electron transport layers (ETL). A thin PCBM layer has also been used on top of the ETL to achieve a better carrier-selective interface with the co-evaporated MAPbI$_3$ absorber layer. Indeed, in agreement with previous results in planar architectures, with spin coated perovskites, [49, 50] the PSCs' PCE significantly improved and the hysteresis reduced, **Figure S1** and **Table S2**. Spiro-oMeTAD has been used as a hole transport layer (HTL) and a 100 nm gold film as the top electrode. Full details of the fabrication process are provided in the experimental section. The vacuum deposition process of hybrid metal-halide perovskite is still challenging due to the need for precise simultaneous control of the evaporation rates of each precursor during the co-evaporation process to reach high quality and well-performing perovskite films. The most critical step is the control of the very volatile MAI within the chamber. To optimize the co-evaporating deposition, the evaporation temperature of PbI$_2$ was fixed at 260 °C and the PbI$_2$:MAI ratio was controlled by changing the MAI evaporation temperature from 90 °C to 120 °C. The thin films were first characterized in terms of morphology, **Figure S2a**, steady-state optical properties (absorption and photoluminescence, PL), **Figure S2b**, and time-resolved PL (TRPL), **Figure S2c.** Subsequently, they were implemented into a solar cell structure, **Figure S3**. Evaporation temperature between 100 °C and 110 °C can guarantee the operation windows where the best device performances and reproducibility can be achieved. Specifically in this work, we kept the MAI evaporation temperature at 100 °C for all the fabrication procedures. Indeed, this condition guarantees a good film quality in terms of morphology and a sharp absorption and the highest PSCs performances can be achieved. **Figure S3**. The X-Ray Diffraction (XRD) spectra of a co-evaporated MAPbI$_3$ thin film at the optimized conditions of 100 °C, presents the polycrystalline MAPbI$_3$ perovskite pattern with intense diffraction peaks at 14.1°, 28.2° and 33.2° corresponding to the (110), (220) and (310) and directions, respectively, **Figure S4a**. A very tiny peak (less than 4% as compared to the perovskite peak) at 12.4° is the PbI$_2$ signature, similarly to what has been observed previously in thermal evaporated MAPbI$_3$ films. [75] The highly asymmetric XRD peak at 14.1° shows that the co-evaporated MAPbI$_3$ is crystallized in the tetragonal phase. Since the XRD measurements have been performed in air

5

and high relative humidity (around 70% RH) conditions, we cannot exclude that the formation of the tetrahedral phase has been accelerated by the environmental conditions as clearly demonstrated by Palazon et al.[76]

To further improve the efficiency of the PSCs, we implemented a surface treatment strategy based on methylammonium iodide (MAI) and potassium acetate (KAc) aiming to improve the charge transport at the grain boundary. [77] The details of the treatment optimization and experimental procedure can be found in the experimental section. The idea is to locally reduce the nonstoichiometric composition which would lead to the presence of under-coordinated species. [78] The evaporation of organic cations and halides can leave few intrinsic point defects, such as Pb–I anti-site defects (PbI_3^-), resulting from growth or processing conditions.[79] These under-coordinated sites are detrimental to the performance of solar cell devices. The introduction of the potassium ion, K^+ in the KAc, can improve the grain boundary conductivity through the immobilization of the uncoordinated species resulting the growth process of the perovskite as the halide excess (I^-) and anti-sites (PbI_3^-) through complexing with potassium on the surface, with a similar mechanism as the one described by Abdi-Jalebi et al. [78] The surface sensitive X-ray photoelectron spectroscopy (XPS) measurements on *treated-MAPbI₃* confirm the presence of K^+ potassium on the thin film surface, **Figure S5.** The time of flight secondary ion mass spectrometry (TOF-SIMS) analysis also shows that the potassium can deeply penetrate homogenously in the films being able to improve the conductivity along with the thick *MAPbI₃* sample, **Figure S6**. The bump of increased potassium intensity at the boundary of perovskite and SnO_2 can be ascribed to interfacial effects as the K^+ ion yields in the two materials, driven by different material properties such as the electron affinity.[80] As expected, the X-Ray Diffraction (XRD) pattern of the *treated*-MAPbI₃ thin film shows a significantly increased perovskite peak, as compared to the pristine MAPbI₃ thin film indicating a better crystallization of the *treated*-MAPbI₃ film and the reduced PbI_2 excess, **Figure 4a**. It is worth to note that from the XRD signal we rule out the presence of KPb_2I_5 as we cannot observe an extra peak around 11.7° after the treatment. Moreover, following Scherrer equation [42], using the full-width half maximum of the peak (110) at 14.1°, it has been possible to estimate larger crystal sizes for the *treated*-MAPbI₃ film as compared to the untreated film, **Figure S4b, and Figure S4c**.

The absorbance spectra of the co-evaporated MAPbI₃ before and after the treatment procedure, **Figure 1b**, presents a sharp absorption peak corresponding to a bandgap of 1.61 eV as estimated from the *Tauc* plot for both the films, **Figure S7**. Consistently the photoluminescence (PL) peak at 780 nm does not shift before and after treatment but the total photoluminescence intensity increases suggesting the effectiveness of the defect passivation and a reduction in non-radiative recombination, as shown in the inset of **Figure 1b**. Similarly, the time-resolved-photoluminescence (TRPL) measurements on MAPbI₃ and *treated*-MAPbI₃ thin-film on glass (**Figure 1c**) show an

enhanced fluorescence lifetime with an average characteristic decay time of ~170 ns to ~360 ns, in agreement with an improved film quality and a low surface and bulk defects density in the treated-MAPbI$_3$ films. The results of the fitting procedure are reported in **Table S3**. The Scanning Electron Microscopy (SEM) images, in the inset of **Figure 1c**, also show that the combined MAI and KAc treatment effectively improved the film morphology as proved by the reduced presence of pin-holes and the increased grain sizes. Indeed, the grain size distributions, Figure **S8** shown that the mean size is around 100 nm and 160 nm for the pristine MAPbI$_3$ and treated-MAPbI$_3$ films respectively. This trend is in agreement with the trend estimated from the XRD spectra in **Figure S4b**. Moreover, the larger grains are visible all through the thickness of the film by the cross-sectional SEM images of the treated films within a device, **Figure S9,** consistently with the deep penetration of the K$^+$ demonstrated by the TOF-SIMS measurements.

Injection properties of co-evaporated MAPbI$_3$ thin film on the electron transport quenching layer have been studied by TRPL. Both ETLs effectively quench the fluorescence emission, reducing the fluorescence lifetimes to 41 ns and 28 ns on TiO$_2$ and SnO$_2$ layer respectively, **Figure S10**. Assuming that charge-carrier quenching occurs only at the extraction layer interface with 100% efficiency we have also estimated an electron diffusion length of 560 nm using a simple diffusion-limited quenching model in a bilayer system.[81] Moreover to investigate the effect of the surface treatment on the MAPbI$_3$ excited states we performed transient absorption spectra of pristine and treated-MAPbI$_3$ films over the same spectral region showing a pronounced photo-bleaching peak band at 770 nm in agreement with the spectral position of the absorption feature and pervious results [82,83], **Figure 1d** and **1e**. The lifetime of the photo-bleaching peak is significantly increased after the MAI+KAc treatment from 100 ns to 320 ns, confirming the effectiveness of the treatment to reduce the charge recombination, **Figure S11** and **Table S4**.

The J-V curves of the champion PSCs including both the pristine MAPbI$_3$ (black line) and the treated-MAPbI$_3$ (blue-line) are reported in **Figure 2a**. The PSC employing a pristine thermally evaporated MAPbI$_3$ reached a PCE of 19.13%, while the treated-MAPbI$_3$ PCS showed a consistent improvement for all photovoltaic parameters (J$_{sc}$, V$_{oc,}$ and FF) achieving a PCE of 19.91%. The complete data sets are reported in **Table 1**. The increased J$_{sc}$ agrees with a charge recombination reduction as proved by the higher PL and the increased TRPL lifetimes. Moreover, both TOF-SIMS and cross-section SEM have shown that the MAI+KAc treatment can penetrate thought all the perovskite films allowing to improve the grain interstitials and also to modify the top and bottom surfaces improving the interfaces with the charge transport layers. Both these effects will lead to an improvement in the FF. A similar effect of post-treatment by anions and cations on improving FF has been reported by Zheng et al..[84] The PSC internal photo conversion efficiency (IPCE) is shown in **Figure S12**.

Consequently, PSCs performances have been further improved to a PCE of 20.28% by introducing a thin layer (100 nm) of LiF as an antireflection coating on top of the glass substrate of the *treated*-MAPbI$_3$ PSC. Indeed, the LiF layers minimize the reflection losses in the PSC, as shown in **Figure S13**, increasing significantly the photons entering in the SCs and consequently maximizing the J$_{sc}$ (from 22.6 to 23.3 mA/cm^2) The statistical distributions of the PCSs PCE realized in three different conditions are shown in **Figure 2b** and the corresponding statistics for all photovoltaic parameters (V$_{oc}$, J$_{sc,}$ and *FF*) of the same cells are reported in **Figure S14**. Moreover, the reverse and forward J-V curves for the champion PSCs in the three different conditions, shown in **Figure S15**, also demonstrated that the K$^+$ addition significantly reduces the hysteresis, in agreement with what has been previously observed for spin-coated PSCs treated with K$^+$. [77,85,86] The figures of merit for the champion PSCs in the three configurations measured in the backward and forward scan and the corresponding hysteresis values are reported in **Table S5** together with mean PCE (PCE$_{mean}$) defined as the mean value of the PCEs measured in both the scanning directions. The PSCs were also studied in the low-intensity illumination regime to investigate the charge recombination behavior for the treated and untreated perovskite. The pristine and *treated*-MAPbI$_3$ PSCs V$_{oc}$ trend as function the light intensity, **Figure S16**, fitted with a linear equation has shown a slop of respectively 1.95 K$_B$T/q and 1.87 K$_B$T/q, where K$_B$ is the Boltzmann constant, T is temperature and q is the electric charge. The smaller slope of *treated*-MAPbI$_3$ PSCs indicates that the charge recombination in perovskite layer was reduced by the treatment.[87] To further probe the effect of our treatment on the charge recombination electrical impedance spectra (EIS) were measured at 0.9 V in dark for both MAPbI$_3$ and *treated*-MAPbI$_3$ PSCs, **Figure 2c**. The EIS were fitted using the equivalent circuit shown in the inset of **Figure 2c**, where R$_{rec}$ represents the perovskite recombination resistance, C$_{con}$ contact capacitance, R$_{dr}$ the dielectric relaxation resistance and C$_{dr}$ capacitance of the perovskite film. [88] In the Nyquist plot both the PSCs show a double circle shape where the low-frequency arc is associated with the dielectric relaxation while the other one to the drift-diffusion/ recombination processes. *Treated*-MAPbI$_3$ PSCs show a significantly larger circle, as compared with the one of the untreated MAPbI$_3$ PSCs, due to a larger R$_{rec}$ consistently with consistent with the reduction of charge recombination observed in the in the *treated-MAPbI$_3$* film as compared to the untreated films.

Moreover, maximum power point tracking under 1 sun illumination of un-encapsulated PSCs proved the enhanced stability of the *treated*-MAPbI$_3$ PSCs as respect to the pure MAPbI$_3$ PSCs, **Figure 2d**. Indeed, the *treated*-MAPbI$_3$ PSCs could retain around 90% of their initial PCE for over 100 hours. The improved stability can be ascribed to the reduction of the under coordinated I$^-$ and anti-sites PbI$_3^-$, by using the K$^+$ treatment, eliminating the defects on the surface and at the interface.[79,89,90] Indeed, the degradation of perovskite films was generally initialized at the defect sites at the film surface and grain boundaries where

the molecules have the highest activity and diffusivity. Thus, the defects passivation at the interface or inside perovskite film could significantly improve device stability. Moreover, contact angle measurements also demonstrate that the *treated*-MAPbI$_3$ samples to be slightly more hydrophobic due to the reduced number of defects, as compared to the respect to the pristine MAPbI$_3$, making it more suitable to humid environments, **Figure S17**.

The state-of-the-art record PCEs values of PSCs have been reported on active areas of ~ 0.1 cm^2 while the increase of the areas generally results in a significant reduction of the PCE as shown by the values reported in **Table S1**. However, to make PSCs suitable and interesting toward commercialization, achieving high PCE on large areas devices is critical. The main reasons behind the consistent efficiency decrease over larger areas are the higher chances of including dust particles and impurities/defects during the solution process preparation procedures, the thin film uniformity reduction, and the electrodes' increased resistivity. In comparison, the thermally evaporated deposition process is performed in intrinsically clean high-vacuum environments which together with the high film uniformity achievable over a large area, this technique complies with the basic requirements for up-scaling the perovskite solar cells technologies. **Figure S18** shows MAPbI$_3$ thin films of different sizes thermally evaporated simultaneously. The cross-sectional SEM images (**Figure S19**) of 4 cm^2 samples show that the perovskite layer thickness at the center and edge (highlighted areas in **Figure S19b** and **Figure S19c**), varies less than 2% over the 4cm^2 active area confirming the good potentiality of deposition technique in fabricating highly efficient large-area devices. For comparison, we have also reported the cross-sectional SEM images for the TiO$_2$ based solar cells, **Figure S20.** This high uniformity on a large area is a key requirement for scaling up the cells and for the possibility to fabricate high-quality perovskite on a standard 6-inch silicon wafer for 2-T perovskite/Silicon tandems, which represent the most promising approach to reach PCEs above 30% while keeping the Levelized Cost Of Energy (LCOE) low.

Figure 3a and **Figure 3b** show the dark, illuminated forward and reverse current density-voltage (J-V) curves of the champion PSCs with 0.16 cm^2, 1 cm^2 and 4 cm^2 active area, incorporating SnO$_2$ and TiO$_2$ as ETL respectively. The photovoltaic values corresponding to the reverse J-V curve are given in **Table 2**. The PSCs employ a *treated*-MAPbI$_3$ and no antireflection coating. The highest PCE of 19.91% is measured on the device with a 0.16 cm^2 active area and SnO$_2$ ETL, while for the same device area with a TiO$_2$ ETL a champion PCE of 18.75% was achieved. Very interestingly, increasing the active areas from 0.16 cm^2 to 1 cm^2 and 4 cm^2 for both the SnO$_2$ and TiO$_2$ both the V$_{oc}$ and J$_{sc}$ remain mostly unaffected, with relative variations between 1 and 2% as compared to the values of the 0.16 cm^2 PSCs. However, the PCE drop for the 4 cm^2 SnO$_2$ based PSCs from the initial 19.91% to 16.59% mainly is due to the FF drop, from 77.89% to 66.11%. Similar effects on the J-V curve properties can be found for the TiO$_2$ devices (**Table 1**). The drop

in *FF* is proportional to the increase in the active area and corresponds to the high resistivity in the transparent conductive oxide (TCO). These data further confirm the good quality and high uniformity of the thermally evaporated $MAPbI_3$ thin films over large areas and confirm that PCE the losses over large areas are ascribable almost entirely to the high electrode resistance. Shelf-stability tests on both TiO_2 and SnO_2-PSCs stored for 110 days in a controlled environment with 35% humidity proved that both PSCs retained 98% and 87% of their initial efficiency respectively, **Figure 3c.**

To minimize the *FF* loss due to the high resistivity of the TCO while moving towards large-area solar devices, we implemented PSM design including 6 sub-cells connected in series. Indeed, the sheet resistance loss can partially be compensated/recovered by connecting thin strips of PSCs, in series connection, into PSMs. The serial connection is however enabled by multiple scribing (commonly known as P1, P2, and P3 scribes) on the PSMs, resulting in an inevitable optical and absorption loss due to the inactive aperture area. Mechanical and laser scribing methods have been previously used to minimize the inactive area, with record Geometrical Fill Factor (GFF) larger than 95%.[35,36]

Generally speaking, the mini-module configuration increases the V_{oc} of the full device and decreases the absolute current flow in the TCO due to the series connection of individual subcells. Consequently, this configuration reduces energy losses due to the increased current and high resistivity over larger areas. To fabricate the PSM the FTO glass was initially etched by an Nd: Yag fiber laser (λ=1064 nm, w=40 µJ) to separate the cells (P1) and create sub-cells with the width of 9 mm. Following the SnO_2, of perovskite and Spiro-OMeTAD depositions, the layers were manually scribed (P2). Finally, a 0.5 mm wide tape was used to form the overall mask (P3) to define the active area before the top electrode deposition. **Figure 4a** shows the image of one PSM with an active area of the 21 cm^2 and the total area 36 cm^2. The PSM J-V measurements are shown in **Figure 4b**. As expected, the V_{oc} could reach 6.71 V indicating that each separate sub-cell delivers on average V_{oc} as high as 1.12 V, consistently with the one measured on small area PSCs. The total current density was 3.68 mA/cm^2, which is equivalent to 22.1 mA/cm^2 in each independent sub-cell, just 2% (0.5 mA/cm^2) lower than the current density values measured on the small area PSCs (**Table 3**, **Figure 3**). The highest PCE of 18.13% has been obtained in the backward scanning mode while PCE_{mean} reached 17.17%.

As we have implemented a narrow strip for each cell and manually scribing, the GFF is just around 72%. Full laser scabbing would allow to further improve the PCE of the PSM. The un-encapsulated module showed good stability retaining above 85% of the initial PCE after 8000s at maximum power point tracking under continuous illumination in high relative humid conditions

(RH=70%), **Figure 4c**. The PSMs showed decent long-term stability in the different conditions analyzed. Indeed, PSMs kept at 65 °C showed an initial fast decrease of PCE followed by a steady behavior maintaining 80 % of the initial PCE after ~100 hours, **Figure 4d**. Additionally, PSMs provide an impressive shelf-stability retaining over 95% of the initial PCE when stored in a controlled environment with 35% humidity throughout ~60 days, **Figure 4e**.

In view of PSCs and PSMs applications in tandem configuration and building integrated photovoltaic, both semi-transparent ST-PSM and ST-PSCs have been fabricated for the first time using a thermal evaporation deposition method. The device architecture is the same as the opaque PSCs and PSMs described earlier, where just the top gold electrode was substituted with a semi-transparent electrode including a 1 nm Ag and a ~195 nm thick ITO layer. [91-93] A 16 cm^2 semi-transparent PSM, **Figure 5a**, achieved a PCE of 11.2% with V_{oc} of 5.65 V (1.13 V for each cell), J_{sc} of 4.11 mA/cm^2 (20.5 mA/cm^2 for each cell) and *FF* of 48.3%, **Figure 5b**. The lower PCE of ST-PSM as compared to the opaque PSM is mainly driven from the drop of J_{sc} (20.5 mA/cm^2 instead of 22.1 mA/cm^2) and *FF* (48.5% instead of 73.44%) ascribable to the reduction of reflection and conductivity of ITO electrode. Further improvement can be achieved by improving ITO conductivity and applying a metal finger electrode on top of ITO. Looking forward to building integrations, colorful ST-PSCs are desirable for many aesthetically appealing architectonics integrations. Here we realized colorful thermally evaporated PSCs just by tuning the thickness of the ITO electrode which consequently modifies the reflection peak of the ST-PSCs.[94] The approach of tuning the transparent electrode thickness appears to be the simplest and most effective way to tune color without introducing additional layers and/or fabrication processes. Maintaining a high and consistent PCE by changing the color appearance of the ST-PSCs can be challenging since light loss due to color reflection and series resistance increase in thin ITO electrodes are difficult to overcome. In this work small devices with an active area of 0.16 cm^2 achieved a champion PCE of 16.83% with V_{oc} of 1.00 V, J_{sc} of 21.9 mA/cm^2, *FF* of 76.83%, **Figure S21**, and with ITO thickness of 210 nm.

Furthermore, varying the ITO thickness from 115 to 220 nm the PSCs PCEs statistics show very consistent values, **Figure 5c**. The statistics of the all photovoltaics parameters are shown in **Figure S22**, confirming that PCE drop is mainly due to the *FF* drop with the increased sheet resistance of the thinner ITO, which can be reduced by introducing metal grids on top of ITO electrode The photovoltaic champion only a slight variation up to 1.5%, as shown in **Table 4**. By changing the ITO thickness, the color of the PSCs can be tuned to produce distinctive colorful hues across the entire visible light spectrum as light-green, orange, pink, violet, blue, deep-green and yellow interestingly, as shown in the inset of **Figure 5c**. The change of color is due to the variation of the

reflectance spectra as shown in **Figure S23**. Their corresponding CIE 1931 color coordinates are reported in **Table 4** and visually represented in **Figure S24**.

Conclusions

In this work, we have shown that our combined effort on thermal evaporation deposition optimization, surface treatment, interfacial passivation, and optical management allowed us to demonstrate MAPbI$_3$ small area evaporated PSCs in n-i-p configuration with PCE of 20.28%. Even more interestingly, scaling the PSCs up to 4 cm^2 we have also not observed any significant losses in the V$_{oc}$ and J$_{sc}$, confirming the high potential of realizing architecture for large-area solar cells. We have also translated the optimized architecture to PSM with an active area of ~ 21 cm^2 which achieved a PCE > 18%. The same device structure can be utilized in fabricating ST-PSCs and ST-PSM with a PCE of 16.8% and 11.2% for active areas of 0.16 cm^2 and 16 cm^2, respectively. For the first time, we also demonstrate thermally co-evaporated colorful PSCs which can deliver consistent PCEs around 16% for a wide range of colors.

To the best of our knowledge, the PCE value of 18.13% for PSMs is among the highest ever reported for perovskite-based devices above 10 cm^2 fabricated with any deposition technique as clearly shown in **Figure 6a** and **Table S1**. Moreover, from a broader perspective, our work clearly shows the proficient scalability of the thermal co-evaporation approach, **Figure 6b**. Indeed, although the PCEs of the thermally co-evaporated PSC$_S$ smaller than 1 cm^2 are still lower than the record values obtained by spin coating for similar sizes, the PCE losses when the sizes are scaled up above 10 cm^2 are considerably smaller than the ones obtained with any other methods (i.e. PCE drop of ~10% for thermally co-evaporation as compared to ~40% for solution-processed devices scaled up from 0.16 cm^2 to 21 cm^2). These results are very promising for the realization for highly efficient modules with typical areas of 256 cm^2.

At the same time, the versatility of the thermal co-evaporation method in realizing semitransparent PSCs and PSMs makes this technology suitable for a variety of applications as tandem solar cells and BIPV, bringing the commercialization of perovskite technology one step closer.

Experimental

Substrate preparation

For single cells, FTO glass (15 Ohm/square) was covered partially by thermal tape and the uncovered area was etched by Zn powder and HCl. For mini-modules: FTO glass (15 Ohm/square) was etched by 1024 nm Nd: Yag fiber LASER. Then the substrates were cleaned by using ultra-sonication with soap (Decon 90) in deionized water, deionized water, and subsequently ethyl alcohol each for 15 min and then

dried by flowing nitrogen gas. This is followed by a UV-ozone treatment (Novascan PSD Pro Series) for 20 min at room temperature.

Electron Transport layer

SnO$_2$: The solution for SnO$_2$ layers was prepared by dissolving 0.05 M SnCl$_2$·2H$_2$O (Sigma-Aldrich) in anhydrous ethanol, then 10 µl of 0.1M InCl$_3$ stock solution in ethanol was added to 1 ml SnCl$_2$ solution to get a 2% (molar ratio) doped SnCl$_2$·2H$_2$O solution. SnO$_2$ layer was prepared by using a two steps spin-coating program (1500 r.p.m. for 10 seconds and 5000 r.p.m. for 10 seconds). The substrate was preheated at 80°C for 10 min and subsequently heated to 180°C for 60 min to convert the SnCl$_2$ to the planar SnO$_2$ layers.

TiO$_2$: The solution for the TiO$_2$ compact layer was prepared by mixing 11g tetrabutyltitnate, 45g anhydrous ethanol, 3.5 g diethanolamine, and 1.5 g deionized water. TiO$_2$ layer was prepared by using a 1 step program (5000 r.p.m. for 20sec). The substrate was preheated at 80°C for 10 min and subsequently heated to 500°C for 60 min to form the planar TiO$_2$ layers.

PCBM: The PCBM solution was made by dissolving 3 mg of PCBM (Sigma) in 1 ml of Chlorobenzene (CBZ) (Sigma-Aldrich). The substrates are treated with UV-Ozone for 20min at 100°C. The PCBM layer is deposited by spin coating PCBM solution at 3000 r.p.m. for 30 seconds.

Perovskite layer

The MAPbI$_3$ perovskite film was deposited on the prepared PCBM/SnO$_2$(TiO$_2$)/FTO glass substrates using a co-evaporation deposition method. The substrates are connected to a rotating (10 rpm) base plate, an average target substrate distance of 30 cm and without temperature control (i.e. floating temperature) in a chamber pumped down to a base pressure of 8*10^{-6} Torr. The perovskite is deposited by co-evaporating PbI$_2$ powder (TCI) and MAI powder (Lumtec) in effusion sources. The PbI$_2$ source was fit at 260°C and MAI source varied from 90, 100, 110 to 120 ^{o}C, respectively, the total deposition time was around 120 min. QCM deposition rates are not given due to the instability of the QCM readings likely caused by an MAI background pressure. The MAPbI$_3$ perovskite film was post-treated by 20 mM KAc and MAI (1:1 in molar ratio) mixed solution in IPA. The as-prepared film and post-treated film were annealed at 100 ^{o}C for 30 min.

Hole Transport Layer and Electrode

The Spiro-OMeTAD solution is prepared by dissolving 72.3 mg of Spiro-oMeTAD powder (Lumtec) in 1 ml of chlorobenzene and stirring it until it is uniform. Add 28.5 ul of TBP solution and 17.5 uL bis(trifluoromethane)sulfonamide lithium salt solution (520mg/ml Li-TFSI in ACN) and stir for 10min. The Spiro-oMeTAD layer is deposited by spin coating at 3000 r.p.m. For single cells, a 100 nm gold electrode was deposited onto the Spiro-OMeTAD layer with difference shape shadow masks by using thermal evaporation or a 200 nm ITO layer was deposited by sputtering. For mini-modules, the P2 process was done by manually scribing, the P3 process was finished by using 0.5 µm wide tape as a mask.

Characterizations

The XRD patterns of the MAPbI$_3$ and *treated*-MAPbI$_3$ thin films (~100 nm thick) were recorded using X-ray diffraction (XRD; Bruker D8 Advance XRD**)**. The XPS spectra were recorded by an X-ray photoelectron spectroscopy (XPS; Kratos AXIS Supra XPS). The film morphology was characterized using SEM (FESEM; JEJOL JSM-7600F). UV-vis absorption spectra and transmittance spectra were taken on a Hitachi U-3501 ultraviolet/visible/near-infrared spectrophotometer. The steady photoluminescence spectra were measured by Spectro-fluorophotometer (Shimadzu, RF-5301PC), under the excitation of 520 nm light source with an intensity of ≈30 mW cm^{-2}.

TRPL dynamics were collected using the micro-PL setup, employing a Nikon microscope, and using a Picoquant PicoHarp 300 time-correlated single-photon counting (TCSPC) system. A picosecond pulsed laser diode, Picoquant P-C-405B, λ = 405 nm with 2.5 MHz repetition (40 Hz frequency divided by a 16 factor) rate has been used as the excitation source. The excitation fluence was <2 □J/cm^2. The emitted fluorescence signal was coupled to an avalanche diode synchronized with excitation laser via TCSPC electronics. Overall, the full width at half maximum of the system instrument response function is around 50 ps.

Transient absorption (TA) measurements MAPbI$_3$ and *treated*-MAPbI$_3$ thin films (~750 nm thick) were performed using Helios (Ultrafast Systems, LLC) pump-probe setup in transmission mode. The 400 nm pump pulses were generated from a 1kHz regenerative amplifier (Coherent Legend, 150 fs, 1 kHz, 800 nm, 1mJ) passing through a BBO crystal by second-harmonic generation. The amplifier was seeded by a mode-locked Ti-sapphire oscillator (Coherent Vitesse, 80 MHz). The white light probe was generated by focusing 800 nm laser onto a 2 mm thick sapphire crystal. A 750 nm short-pass filter was placed before the probe focusing onto the sample. Also, a 450 nm long-pass filter was used to block the excitation beam from entering the detector. By chopping the pump and adjusting the time delay between pump and probe, only pumped induced transmission change in the white light spectrum can be collected. The excitation fluence was 1.7 □J/cm^2

The current density–voltage (J–V) curves were measured under simulated AM 1.5 sunlight (Newport) which is calibrated by a standard silicon solar cell. The effective areas were determined by metal aperture masks with different size for J-V measurement. The incident photon-to-current conversion efficiency (IPCE) was measured by using a PVE300 (Bentham), with a dual xenon/quartz halogen light source in DC mode Newport Oriel Sol3A^{TM} solar simulator with a 450-watt Xenon lamp. Dark scan 1.2 V to -0.1 V. Forward scan -0.1V to 1.2V. Reverse scan 1.2 V to -0.1 V. The EIS spectra and stabilized power output track are measured by an Autolab machine (PGSTAT302N, Software version- NOVA 1.11).

Conflict of Interests

Two of the authors N.M. and S.M. are directors of Prominence Photovoltaics Pte Ltd a perovskite solar cell commercialization company. The other authors have no conflict of interests to declare

Acknowledgments

Authors Contributions

A.B., S.M., and N.M. conceived and planned the experiments. L.J., K.V. developed the perovskite deposition process by thermal evaporation with the support and suggestions of H.B. L.J. fabricated the PSC and the PSM. X.Y. supported the fabrication of the device. W.H. fabricated the colored ST-PSC. H.D. characterized thin films. T.W.G., J.W.M.L. and T.C.S. performed the TA measurements. A.B. and C.S. took care of the TRPL. J.H.L. performed the module laser scribing. A.B. wrote the first version of the manuscript. A.B. and L.J. and X.Y. finalized the manuscript with inputs from all the authors.

References

1. https://ec.europa.eu/clima/policies/international/negotiations/paris_en.
2. Kim, H.S., Lee, C.R., Im, J.H., Lee, K.B., Moehl, T., Marchioro, A., Moon, S.J., Humphry-Baker, R., Yum, J.H., Moser, J.E*., et al.* (2012). Lead iodide perovskite sensitized all-solid-state submicron thin film mesoscopic solar cell with efficiency exceeding 9%. Scientific reports *2*, 591.
3. Lee, M.M., Teuscher, J., Miyasaka, T., Murakami, T.N., and Snaith, H.J. (2012). Efficient hybrid solar cells based on meso-superstructured organometal halide perovskites. Science *338*, 643-647.
4. Yang, W.S., Park, B.-W., Jung, E.H., Jeon, N.J., Kim, Y.C., Lee, D.U., Shin, S.S., Seo, J., Kim, E.K., and Noh, J.H. (2017). Iodide management in formamidinium-lead-halide–based perovskite layers for efficient solar cells. Science *356*, 1376-1379.
5. Jung, E.H., Jeon, N.J., Park, E.Y., Moon, C.S., Shin, T.J., Yang, T.-Y., Noh, J.H., and Seo, J. (2019). Efficient, stable and scalable perovskite solar cells using poly (3-hexylthiophene). Nature *567*, 511.
6. Chin, X.Y., Cortecchia, D., Yin, J., Bruno, A., and Soci, C. (2015). Lead iodide perovskite light-emitting field-effect transistor. Nature communications *6*, 7383.
7. Chin, X.Y., Perumal, A., Bruno, A., Yantara, N., Veldhuis, S.A., Martínez-Sarti, L., Chandran, B., Chirvony, V., Lo, A.S.-Z., and So, J. (2018). Self-assembled hierarchical nanostructured perovskites enable highly efficient LEDs via an energy cascade. Energy & Environmental Science *11*, 1770-1778.

8. Saliba, M., Matsui, T., Seo, J.-Y., Domanski, K., Correa-Baena, J.-P., Nazeeruddin, M.K., Zakeeruddin, S.M., Tress, W., Abate, A., Hagfeldt, A.*, et al.* (2016). Cesium-containing triple cation perovskite solar cells: improved stability, reproducibility and high efficiency. Energy & Environmental Science *9*, 1989-1997.

9. Green, M.A., Ho-Baillie, A., and Snaith, H.J. (2014). The emergence of perovskite solar cells. Nature photonics *8*, 506.

10. De Wolf, S., Holovsky, J., Moon, S.J., Loper, P., Niesen, B., Ledinsky, M., Haug, F.J., Yum, J.H., and Ballif, C. (2014). Organometallic Halide Perovskites: Sharp Optical Absorption Edge and Its Relation to Photovoltaic Performance. The journal of physical chemistry letters *5*, 1035-1039.

11. Shi, D., Adinolfi, V., Comin, R., Yuan, M., Alarousu, E., Buin, A., Chen, Y., Hoogland, S., Rothenberger, A., Katsiev, K.*, et al.* (2015). Low trap-state density and long carrier diffusion in organolead trihalide perovskite single crystals. Science *347*, 519-522.

12. Stranks, S.D., Eperon, G.E., Grancini, G., Menelaou, C., Alcocer, M.J.P., Leijtens, T., Herz, L.M., Petrozza, A., and Snaith, H.J. (2013). Electron-Hole Diffusion Lengths Exceeding 1 Micrometer in an Organometal Trihalide Perovskite Absorber. Science *342*, 341-344.

13. Xing, G., Mathews, N., Sun, S., Lim, S., Lam, Y., Grätzel, M., Mhaisalkar, S., Sum, T., and Gratzel, M. (2013). Long-Range Balanced Electron- and Hole-Transport Lengths in Organic-Inorganic $CH_3NH_3PbI_3$. Science *342*, 344-347.

14. Dong, Q., Fang, Y., Shao, Y., Mulligan, P., Qiu, J., Cao, L., and Huang, J. (2015). Electron-hole diffusion lengths > 175 μm in solution-grown $CH_3NH_3PbI_3$ single crystals. Science *347*, 967-970.

15. Zheng, L., Zhang, D., Ma, Y., Lu, Z., Chen, Z., Wang, S., Xiao, L., and Gong, Q. (2015). Morphology control of the perovskite films for efficient solar cells. Dalton transactions *44*, 10582-10593.

16. Zhao, Y., and Zhu, K. (2016). Organic–inorganic hybrid lead halide perovskites for optoelectronic and electronic applications. Chemical Society Reviews *45*, 655-689.

17. Dang, Y., Ju, D., Wang, L., and Tao, X. (2016). Recent progress in the synthesis of hybrid halide perovskite single crystals. CrystEngComm *18*, 4476-4484.

18. Kojima, A., Teshima, K., Shirai, Y., and Miyasaka, T. (2009). Organometal Halide Perovskites as Visible-Light Sensitizers for Photovoltaic Cells. Journal of the American Chemical Society *131*, 6050-6051.

19. Fei, C., Li, B., Zhang, R., Fu, H., Tian, J., and Cao, G. (2017). Highly Efficient and Stable Perovskite Solar Cells Based on Monolithically Grained $CH_3NH_3PbI_3$ Film. Advanced Energy Materials *7*, 1602017.

20. Nogay, G., Sahli, F., Werner, J., Monnard, R., Boccard, M., Despeisse, M., Haug, F.J., Jeangros, Q., Ingenito, A., and Ballif, C. (2019). 25.1%-Efficient Monolithic Perovskite/Silicon Tandem Solar Cell Based on a p-type Monocrystalline Textured Silicon Wafer and High-Temperature Passivating Contacts. Acs Energy Letters *4*, 844-845.

21. Sahli, F., Werner, J., Kamino, B.A., Brauninger, M., Monnard, R., Paviet-Salomon, B., Barraud, L., Ding, L., Diaz Leon, J.J., Sacchetto, D.*, et al.* (2018). Fully textured monolithic perovskite/silicon tandem solar cells with 25.2% power conversion efficiency. Nature Materials *17*, 820-826.

22. Sahli, F., Kamino, B.A., Werner, J., Brauninger, M., Paviet-Salomon, B., Barraud, L., Monnard, R., Seif, J.P., Tomasi, A., Jeangros, Q.*, et al.* (2018). Improved Optics in Monolithic Perovskite/Silicon Tandem Solar Cells with a Nanocrystalline Silicon Recombination Junction. Advanced Energy Materials *8,* 1701609.

23. Werner, J., Niesen, B., and Ballif, C. (2018). Perovskite/Silicon Tandem Solar Cells: Marriage of Convenience or True Love Story? - An Overview. Advanced Materials Interfaces *5,* 1700731.

24. Jaysankar, M., Raul, B.A.L., Bastos, J., Burgess, C., Weijtens, C., Creatore, M., Aernouts, T., Kuang, Y., Gehlhaar, R., Hadipour, A.*, et al.* (2018). Minimizing Voltage Loss in Wide-Bandgap Perovskites for Tandem Solar Cells. ACS Energy Letters, 259-264.

25. Duong, T., Wu, Y., Shen, H., Peng, J., Fu, X., Jacobs, D., Wang, E.-C., Kho, T.C., Fong, K.C., Stocks, M.*, et al.* (2017). Rubidium Multication Perovskite with Optimized Bandgap for Perovskite-Silicon Tandem with over 26% Efficiency. Advanced Energy Materials *7,* 1700228.

26. Bush, K.A., Palmstrom, A.F., Yu, Z.J., Boccard, M., Cheacharoen, R., Mailoa, J.P., McMeekin, D.P., Hoye, R.L.Z., Bailie, C.D., Leijtens, T.*, et al.* (2017). 23.6%-efficient monolithic perovskite/silicon tandem solar cells with improved stability. Nature Energy *2,* 1-7.

27. Forgács, D., Gil-Escrig, L., Pérez-Del-Rey, D., Momblona, C., Werner, J., Niesen, B., Ballif, C., Sessolo, M., and Bolink, H.J. (2017). Efficient Monolithic Perovskite/Perovskite Tandem Solar Cells. Advanced Energy Materials *7*, 1602121.

28. Zhang, W., Anaya, M., Lozano, G., Calvo, M.E., Johnston, M.B., Míguez, H., and Snaith, H.J. (2015). Highly Efficient Perovskite Solar Cells with Tunable Structural Color. Nano letters *15*, 1698-1702.

29. Xue, Q., Xia, R., Brabec, C.J., and Yip, H.-L. (2018). Recent advances in semi-transparent polymer and perovskite solar cells for power generating window applications. Energy & Environmental Science *11*, 1688-1709.

30. Yang, W.S., Noh, J.H., Jeon, N.J., Kim, Y.C., Ryu, S., Seo, J., and Seok, S.I. (2015). High-performance photovoltaic perovskite layers fabricated through intramolecular exchange. Science *348*, 1234-1237.

31. Bi, D., Tress, W., Dar, M.I., Gao, P., Luo, J., Renevier, C., Schenk, K., Abate, A., Giordano, F., Correa Baena, J.-P.*, et al.* (2016). Efficient luminescent solar cells based on tailored mixed-cation perovskites. Science Advances *2*, e1501170.

32. Saliba, M., Matsui, T., Seo, J.-Y., Domanski, K., Correa-Baena, J.-P., Nazeeruddin, M.K., Zakeeruddin, S.M., Tress, W., Abate, A., Hagfeldt, A.*, et al.* (2016). Cesium-containing triple cation perovskite solar cells: improved stability, reproducibility and high efficiency. Energy & Environmental Science *9*, 1989-1997.

33. Saliba, M., Matsui, T., Domanski, K., Seo, J.-Y., Ummadisingu, A., Zakeeruddin, S.M., Correa-Baena, J.-P., Tress, W.R., Abate, A., Hagfeldt, A.*, et al.* (2016). Incorporation of rubidium cations into perovskite solar cells improves photovoltaic performance. Science *354*, 206-209.

34. McMeekin, D.P., Sadoughi, G., Rehman, W., Eperon, G.E., Saliba, M., Hörantner, M.T., Haghighirad, A., Sakai, N., Korte, L., Rech, B.*, et al.* (2016). A mixed-cation lead mixed-halide perovskite absorber for tandem solar cells. Science *351*, 151-155.

35. Moon, S., Yum, J., Löfgren, L., Walter, A., Sansonnens, L., Benkhaira, M., Nicolay, S., Bailat, J., and Ballif, C. (2015). Laser-Scribing Patterning for the Production of Organometallic Halide Perovskite Solar Modules. IEEE Journal of Photovoltaics *5*, 1087-1092.

36. Palma, A.L., Matteocci, F., Agresti, A., Pescetelli, S., Calabrò, E., Vesce, L., Christiansen, S., Schmidt, M., and Carlo, A.D. (2017). Laser-Patterning Engineering for Perovskite Solar Modules With 95% Aperture Ratio. IEEE Journal of Photovoltaics *7*, 1674-1680.

37. Yang, M., Li, Z., Reese, M.O., Reid, O.G., Kim, D.H., Siol, S., Klein, T.R., Yan, Y., Berry, J.J., van Hest, M.F.A.M.*, et al.* (2017). Perovskite ink with wide processing window for scalable high-efficiency solar cells. Nature Energy *2*, 17038.

38. Deng, Y., Zheng, X., Bai, Y., Wang, Q., Zhao, J., and Huang, J. (2018). Surfactant-controlled ink drying enables high-speed deposition of perovskite films for efficient photovoltaic modules. Nature Energy *3*, 560-566.

39. Yang, M., Kim, D.H., Klein, T.R., Li, Z., Reese, M.O., Tremolet de Villers, B.J., Berry, J.J., van Hest, M.F.A.M., and Zhu, K. (2018). Highly Efficient Perovskite Solar Modules by Scalable Fabrication and Interconnection Optimization. ACS Energy Letters *3*, 322-328.

40. Razza, S., Di Giacomo, F., Matteocci, F., Cinà, L., Palma, A.L., Casaluci, S., Cameron, P., D'Epifanio, A., Licoccia, S., Reale, A.*, et al.* (2015). Perovskite solar cells and large area modules (100 cm^2) based on an air flow-assisted PbI$_2$ blade coating deposition process. Journal of Power Sources *277*, 286-291.

41. Deng, Y., Van Brackle, C.H., Dai, X., Zhao, J., Chen, B., and Huang, J. (2019). Tailoring solvent coordination for high-speed, room-temperature blading of perovskite photovoltaic films. Science advances *5*, eaax7537.

42. Heo, J.H., Lee, M.H., Jang, M.H., and Im, S.H. (2016). Highly efficient CH$_3$NH$_3$PbI$_{3-x}$Cl$_x$ mixed halide perovskite solar cells prepared by re-dissolution and crystal grain growth via spray coating. Journal of Materials Chemistry A *4*, 17636-17642.

43. Di Giacomo, F., Shanmugam, S., Fledderus, H., Bruijnaers, B.J., Verhees, W.J.H., Dorenkamper, M.S., Veenstra, S.C., Qiu, W., Gehlhaar, R., Merckx, T.*, et al.* (2018). Up-scalable sheet-to-sheet production of high efficiency perovskite module and solar cells on 6-in. substrate using slot die coating. Solar Energy Materials and Solar Cells *181*, 53-59.

44. Cai, L., Liang, L., Wu, J., Ding, B., Gao, L., and Fan, B. (2017). Large area perovskite solar cell module. Journal of Semiconductors *38*, 014006.

45. Bu, T., Liu, X., Zhou, Y., Yi, J., Huang, X., Luo, L., Xiao, J., Ku, Z., Peng, Y., Huang, F., *et al.* (2017). A novel quadruple-cation absorber for universal hysteresis elimination for high efficiency and stable perovskite solar cells. Energy & Environmental Science *10*, 2509-2515.

46. Han, G.S., Kim, J., Bae, S., Han, S.-H., Kim, Y.J., Gong, O.Y., Lee, P., Ko, M.J., and Jung, H.S. (2019). Spin Coating Process for 10 cm × 10 cm Perovskite Solar Modules Enabled by Self-Assembly of SnO_2 Nanocolloids. ACS Energy Letters *4*, 1845-1851.

47. Agresti, A., Pescetelli, S., Palma, A.L., Martin-Garcia, B., Najafi, L., Bellani, S., Moreels, I., Prato, M., Bonaccorso, F., and Di Carlo, A. (2019). Two-dimensional (2D) Material Interface Engineering for Efficient Perovskite Large-area Modules. ACS Energy Letters *4*, 1862-1871.

48. Bu, T., Li, J., Zheng, F., Chen, W., Wen, X., Ku, Z., Peng, Y., Zhong, J., Cheng, Y.-B., and Huang, F. (2018). Universal passivation strategy to slot-die printed SnO2 for hysteresis-free efficient flexible perovskite solar module. Nature Communications *9*, 4609.

49. Kim, J., Yun, J.S., Cho, Y., Lee, D.S., Wilkinson, B., Soufiani, A.M., Deng, X., Zheng, J., Shi, A., Lim, S., *et al.* (2017). Overcoming the Challenges of Large-Area High-Efficiency Perovskite Solar Cells. ACS Energy Letters *2*, 1978-1984.

50. Jaysankar, M., Paetel, S., Ahlswede, E., Paetzold, U.W., Aernouts, T., Gehlhaar, R., and Poortmans, J. (2019). Toward scalable perovskite-based multijunction solar modules. Progress in Photovoltaics: Research and Applications *27*, 733-738.

51. Calabrò, E., Matteocci, F., Palma, A.L., Vesce, L., Taheri, B., Carlini, L., Pis, I., Nappini, S., Dagar, J., Battocchio, C., *et al.* (2018). Low temperature, solution-processed perovskite solar cells and modules with an aperture area efficiency of 11%. Solar Energy Materials and Solar Cells *185*, 136-144.

52. Troughton, J., Hooper, K., and Watson, T.M. (2017). Humidity resistant fabrication of $CH_3NH_3PbI_3$ perovskite solar cells and modules. Nano Energy *39*, 60-68.

53. Bu, T., Shi, S., Li, J., Liu, Y., Shi, J., Chen, L., Liu, X., Qiu, J., Ku, Z., Peng, Y., *et al.* (2018). Low-Temperature Presynthesized Crystalline Tin Oxide for Efficient Flexible Perovskite Solar Cells and Modules. ACS applied materials & interfaces *10*, 14922-14929.

54. Huang, Z., Hu, X., Liu, C., Meng, X., Huang, Z., Yang, J., Duan, X., Long, J., Zhao, Z., Tan, L., *et al.* (2019) Water-Resistant and Flexible Perovskite Solar Cells via a Glued Interfacial Layer. Advanced Functional Materials *29*, 1902629.

55. Bu, T., Wu, L., Liu, X., Yang, X., Zhou, P., Yu, X., Qin, T., Shi, J., Wang, S., Li, S., *et al.* (2017). Synergic Interface Optimization with Green Solvent Engineering in Mixed Perovskite Solar Cells. Advanced Energy Materials *7*, 1700576.

56. Qiu, W., Merckx, T., Jaysankar, M., Masse de la Huerta, C., Rakocevic, L., Zhang, W., Paetzold, U.W., Gehlhaar, R., Froyen, L., Poortmans, J., *et al.* (2016). Pinhole-free perovskite films for efficient solar modules. Energy & Environmental Science *9*, 484-489.

57. Yeo, J.-S., Lee, C.-H., Jang, D., Lee, S., Jo, S.M., Joh, H.-I., and Kim, D.-Y. (2016). Reduced graphene oxide-assisted crystallization of perovskite via solution-process for efficient and stable planar solar cells with module-scales. Nano Energy *30*, 667-676.

58. Heo, J.H., Han, H.J., Kim, D., Ahn, T.K., and Im, S.H. (2015). Hysteresis-less inverted $CH_3NH_3PbI_3$ planar perovskite hybrid solar cells with 18.1% power conversion efficiency. Energy & Environmental Science *8*, 1602-1608.

59. Jung, E.H., Jeon, N.J., Park, E.Y., Moon, C.S., Shin, T.J., Yang, T.-Y., Noh, J.H., and Seo, J. (2019). Efficient, stable and scalable perovskite solar cells using poly(3-hexylthiophene). Nature *567*, 511-515.

60. Chiang, C.-H., Nazeeruddin, M.K., Grätzel, M., and Wu, C.-G. (2017). The synergistic effect of H_2O and DMF towards stable and 20% efficiency inverted perovskite solar cells. Energy & Environmental Science *10*, 808-817.

61. Qiu, L., Liu, Z., Ono, L.K., Jiang, Y., Son, D.-Y., Hawash, Z., He, S., and Qi, Y. (2018). Scalable Fabrication of Stable High Efficiency Perovskite Solar Cells and Modules Utilizing Room Temperature Sputtered SnO_2 Electron Transport Layer. Advanced Functional Materials *29*, 1806779.

62. Liu, Z., Qiu, L., Juarez-Perez, E.J., Hawash, Z., Kim, T., Jiang, Y., Wu, Z., Raga, S.R., Ono, L.K., Liu, S., *et al.* (2018). Gas-solid reaction based over one-micrometer thick stable perovskite films for efficient solar cells and modules. Nature communications *9*, 3880.

63. Liao, H.-C., Guo, P., Hsu, C.-P., Lin, M., Wang, B., Zeng, L., Huang, W., Soe, C.M.M., Su, W.-F., Bedzyk, M.J.*, et al.* (2017). Enhanced Efficiency of Hot-Cast Large-Area Planar Perovskite Solar Cells/Modules Having Controlled Chloride Incorporation. Advanced Energy Materials *7*, 1601660.

64. Leyden, M.R., Jiang, Y., and Qi, Y. (2016). Chemical vapor deposition grown formamidinium perovskite solar modules with high steady state power and thermal stability. Journal of Materials Chemistry A *4*, 13125-13132.

65. Jiang, Y., Leyden, M.R., Qiu, L., Wang, S., Ono, L.K., Wu, Z., Juarez-Perez, E.J., and Qi, Y. (2018). Combination of Hybrid CVD and Cation Exchange for Upscaling Cs-Substituted Mixed Cation Perovskite Solar Cells with High Efficiency and Stability. Advanced Functional Materials *28,* 1703835.

66. Chen, H., Ye, F., Tang, W., He, J., Yin, M., Wang, Y., Xie, F., Bi, E., Yang, X., Gratzel, M.*, et al.* (2017). A solvent- and vacuum-free route to large-area perovskite films for efficient solar modules. Nature *550,* 92-95.

67. Agresti, A., Pescetelli, S., Palma, A.L., Del Rio Castillo, A.E., Konios, D., Kakavelakis, G., Razza, S., Cinà, L., Kymakis, E., Bonaccorso, F.*, et al.* (2017). Graphene Interface Engineering for Perovskite Solar Modules: 12.6% Power Conversion Efficiency over 50 cm^2 Active Area. ACS Energy Letters *2*, 279-287.

68. Deng, Y., Zheng, X., Bai, Y., Wang, Q., Zhao, J., and Huang, J. (2018). Surfactant-controlled ink drying enables high-speed deposition of perovskite films for efficient photovoltaic modules. Nature Energy *3*, 560.

69. Grancini, G., Roldán-Carmona, C., Zimmermann, I., Mosconi, E., Lee, X., Martineau, D., Narbey, S., Oswald, F., De Angelis, F., Graetzel, M.*, et al.* (2017). One-Year stable perovskite solar cells by 2D/3D interface engineering. Nature communications *8*, 15684.

70. Liu, M., Johnston, M.B., and Snaith, H.J. (2013). Efficient planar heterojunction perovskite solar cells by vapour deposition. Nature *501*, 395-398.

71. Momblona, C., Gil-Escrig, L., Bandiello, E., Hutter, E.M., Sessolo, M., Lederer, K., Blochwitz-Nimoth, J., and Bolink, H.J. (2016). Efficient vacuum deposited p-i-n and n-i-p perovskite solar cells employing doped charge transport layers. Energy & Environmental Science *9*, 3456-3463.

72. Gil-Escrig, L., Momblona, C., La-Placa, M.-G., Boix, P.P., Sessolo, M., and Bolink, H.J. (2018). Vacuum Deposited Triple-Cation Mixed-Halide Perovskite Solar Cells. Advanced Energy Materials *8*, 1703506.

73. Turkevych, I., Kazaoui, S., Belich, N.A., Grishko, A.Y., Fateev, S.A., Petrov, A.A., Urano, T., Aramaki, S., Kosar, S., Kondo, M.*, et al.* (2018). Strategic advantages of reactive polyiodide melts for scalable perovskite photovoltaics. Nature nanotechnology *14*, 57-63.

74. Werner, J., Sahli, F., Fu, F., Leon, J.J.D., Walter, A., Kamino, B.A., Niesen, B., Nicolay, S., Jeangros, Q., and Ballif, C. (2018). Perovskite/Perovskite/Silicon Monolithic Triple-Junction Solar Cells with a Fully Textured Design. Acs Energy Letters *3*, 2052-2058.

75. Liu, M., Johnston, M.B., and Snaith, H.J. (2013). Efficient planar heterojunction perovskite solar cells by vapour deposition. Nature *501*, 395-398.

76. Palazon, F., PérezdelRey, D., Dänekamp, B., Dreessen, C., Sessolo, M., Boix, P.P., and Bolink, H.J. (2019). Room-Temperature Cubic Phase Crystallization and High Stability of Vacuum-Deposited Methylammonium Lead Triiodide Thin Films for High-Efficiency Solar Cells. Advanced materials *31*, 1902692.

77. Abdi-Jalebi, M., Andaji-Garmaroudi, Z., Cacovich, S., Stavrakas, C., Philippe, B., Richter, J.M., Alsari, M., Booker, E.P., Hutter, E.M., Pearson, A.J.*, et al.* (2018). Maximizing and stabilizing luminescence from halide perovskites with potassium passivation. Nature *555*, 497.

78. Abdi-Jalebi, M., Andaji-Garmaroudi, Z., Cacovich, S., Stavrakas, C., Philippe, B., Richter, J.M., Alsari, M., Booker, E.P., Hutter, E.M., Pearson, A.J.*, et al.* (2018). Maximizing and stabilizing luminescence from halide perovskites with potassium passivation. Nature *555*, 497-501.

79. Chen, B., Rudd, P.N., Yang, S., Yuan, Y., and Huang, J. (2019). Imperfections and their passivation in halide perovskite solar cells. Chemical Society Reviews *48*, 3842-3867.

80. Zhou, Y., Yao, J., Ding, Y., Yu, J., Hua, X., Evans, J.E., Yu, X., Lao, D.B., Heldebrant, D.J., and Nune, S.K. (2016). Improving the molecular ion signal intensity for in situ liquid SIMS analysis. Journal of The American Society for Mass Spectrometry *27*, 2006-2013.

81. Xing, G., Mathews, N., Sun, S., Lim, S.S., Lam, Y.M., Grätzel, M., Mhaisalkar, S., and Sum, T.C. (2013). Long-Range Balanced Electron- and Hole-Transport Lengths in Organic-Inorganic $CH_3NH_3PbI_3$. Science *342*, 344-347.

82. Xing, G., Mathews, N., Sun, S., Lim, S.S., Lam, Y.M., Gratzel, M., Mhaisalkar, S., and Sum, T.C. (2013). Long-range balanced electron- and hole-transport lengths in organic-inorganic $CH_3NH_3PbI_3$. Science *342*, 344-347.

83. Sum, T.C., and Mathews, N. (2014). Advancements in perovskite solar cells: photophysics behind the photovoltaics. Energy & Environmental Science *7*, 2518-2534.

84. Zheng, X., Chen, B., Dai, J., Fang, Y., Bai, Y., Lin, Y., Wei, H., Zeng, Xiao C., and Huang, J. (2017). Defect passivation in hybrid perovskite solar cells using quaternary ammonium halide anions and cations. Nature Energy *2*, 17102.

85. Tang, Z., Bessho, T., Awai, F., Kinoshita, T., Maitani, M.M., Jono, R., Murakami, T.N., Wang, H., Kubo, T., and Uchida, S. (2017). Hysteresis-free perovskite solar cells made of potassium-doped organometal halide perovskite. Scientific reports *7*, 12183.

86. Zheng, F., Chen, W., Bu, T., Ghiggino, K.P., Huang, F., Cheng, Y., Tapping, P., Kee, T.W., Jia, B., and Wen, X. (2019). Triggering the Passivation Effect of Potassium Doping in Mixed-Cation Mixed-Halide Perovskite by Light Illumination. Advanced Energy Materials, *9* 1901016.

87. Jiang, Q., Zhao, Y., Zhang, X., Yang, X., Chen, Y., Chu, Z., Ye, Q., Li, X., Yin, Z., and You, J. (2019). Surface passivation of perovskite film for efficient solar cells. Nature Photonics *13*, 460-466.

88. Yoo, S.-M., Yoon, S.J., Anta, J.A., Lee, H.J., Boix, P.P., and Mora-Seró, I. (2019). An Equivalent Circuit for Perovskite Solar Cell Bridging Sensitized to Thin Film Architectures. Joule *3,* 2535-2549.

89. Zheng, X., Chen, B., Dai, J., Fang, Y., Bai, Y., Lin, Y., Wei, H., Zeng, X.C., and Huang, J. (2017). Defect passivation in hybrid perovskite solar cells using quaternary ammonium halide anions and cations. Nature Energy *2*, 17102.

90. Tan, H.R., Jain, A., Voznyy, O., Lan, X.Z., de Arquer, F.P.G., Fan, J.Z., Quintero-Bermudez, R., Yuan, M.J., Zhang, B., Zhao, Y.C.*, et al.* (2017). Efficient and stable solution-processed planar perovskite solar cells via contact passivation. Science *355*, 722-726.

91. Dewi, H.A., Wang, H., Li, J., Thway, M., Sridharan, R., Stangl, R., Lin, F., Aberle, A.G., Mathews, N., and Bruno, A. (2019). Highly Efficient Semi-Transparent Perovskite Solar Cells for Four Terminal Perovskite-Silicon Tandems. ACS applied materials & interfaces *11,* 34178-34187.

92. Guchhait, A., Dewi, H.A., Leow, S.W., Wang, H., Han, G., Suhaimi, F.B., Mhaisalkar, S., Wong, L.H., and Mathews, N. (2017). Over 20% efficient CIGS–perovskite tandem solar cells. ACS Energy Letters *2*, 807-812.

93. Dewi, H.A., Wang, H., Li, J., Thway, M., Lin, F., Aberle, A.G., Mathews, N., Mhaisalkar, S., and Bruno, A. (2020). Four-Terminal Perovskite on Silicon Tandem Solar Cells Optimal Measurements Schemes. Energy Technology.

94. Wang, H., Dewi, H.A., Koh, T.M., Bruno, A., Mhaisalkar, S.G., and Mathews, N. (2020). Bifacial, Color-Tunable Semitransparent Perovskite Solar Cells for Building Integrated Photovoltaics. ACS applied materials & interfaces *12*, 484-493.
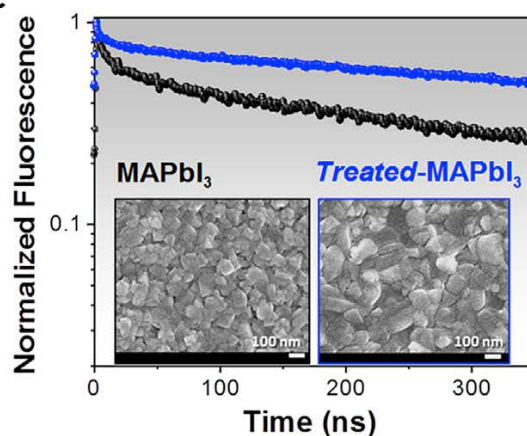
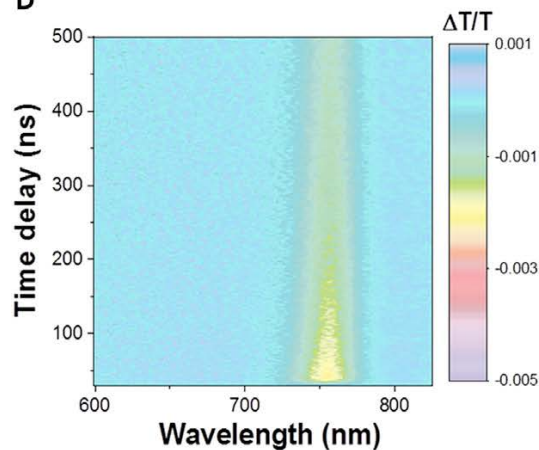# Main Figures Titles and Legends
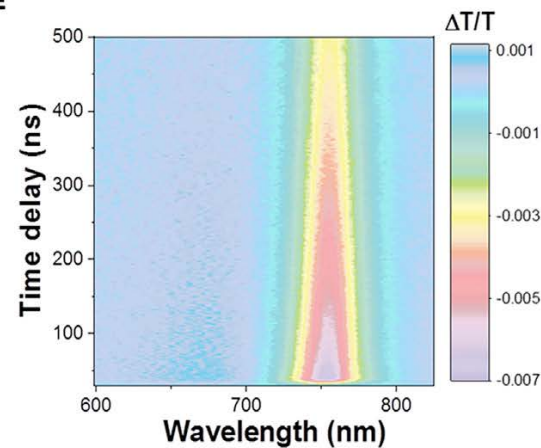
A
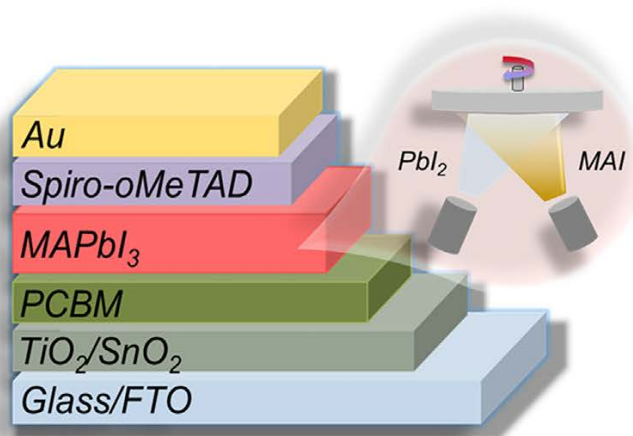
B
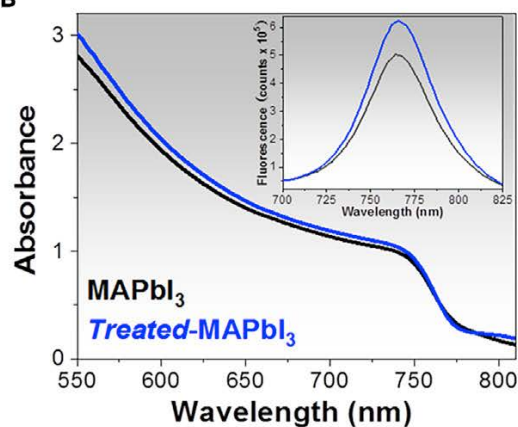
C

D

E

Figure 1: Thermally co-evaporated MAPbI₃ thin films. (a) The schematic architecture of the planar PSC layers stack. The inset shows a schematic illustration of the PbI₂ and MAI thermal co-evaporation process. Thermally evaporated pristine MAPbI₃ (black line), *treated*-MAPbI₃ (blue line) thin films characterizations: (b) absorption and PL spectra (in the inset); (c) TRPL decays. Top-view SEM images are reported in the inset. Transient absorption spectra temporal evolution of (d) thermally evaporated MAPbI₃ and (e) *treated*-MAPbI₃ films. (see also **Figure S4, Figure S5, Figure S6, Figure S7, Figure S8**, **Figure S9, Figure S10, Figure S11**, **Table S1** and **Table S4**)
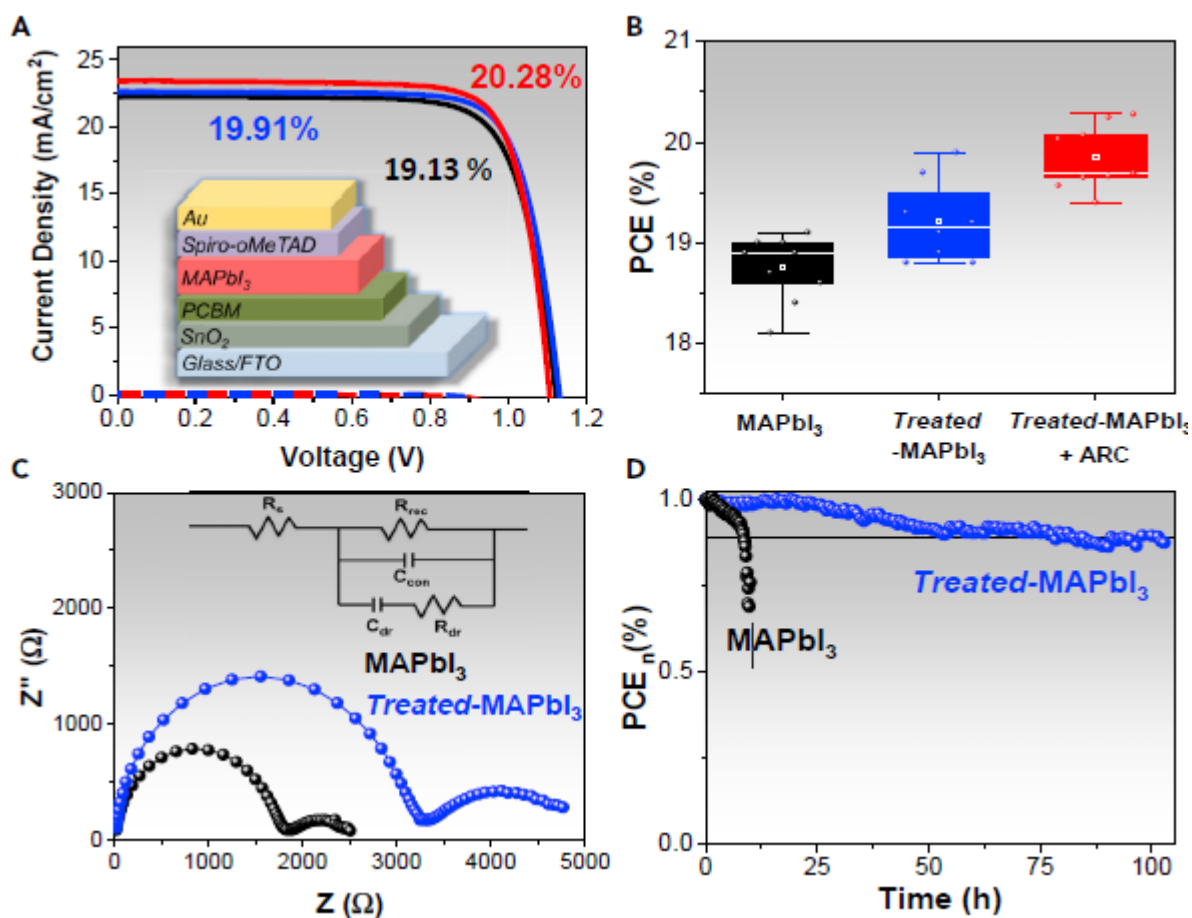
Figure 2: Thermally evaporated MAPbI₃ planar PSCs. (a) champion PSCs J-V curves in backwards scanning mode; (b) PCEs statistical distributions; (c) Nyquist plots measured at 0.9 V in dark and (d) normalised PCE (PCEn) versus time under continuous illumination in nitrogen for PSCs with pristine thermally evaporated MAPbI₃ (black), *treated*-MAPbI₃ (blue) and *treated*-MAPbI₃+ LiF antireflection coating (red). (see also **Figure S12, Figure S13, Figure S14, Figure S15, Figure S16, Figure S17 and Table S5**)
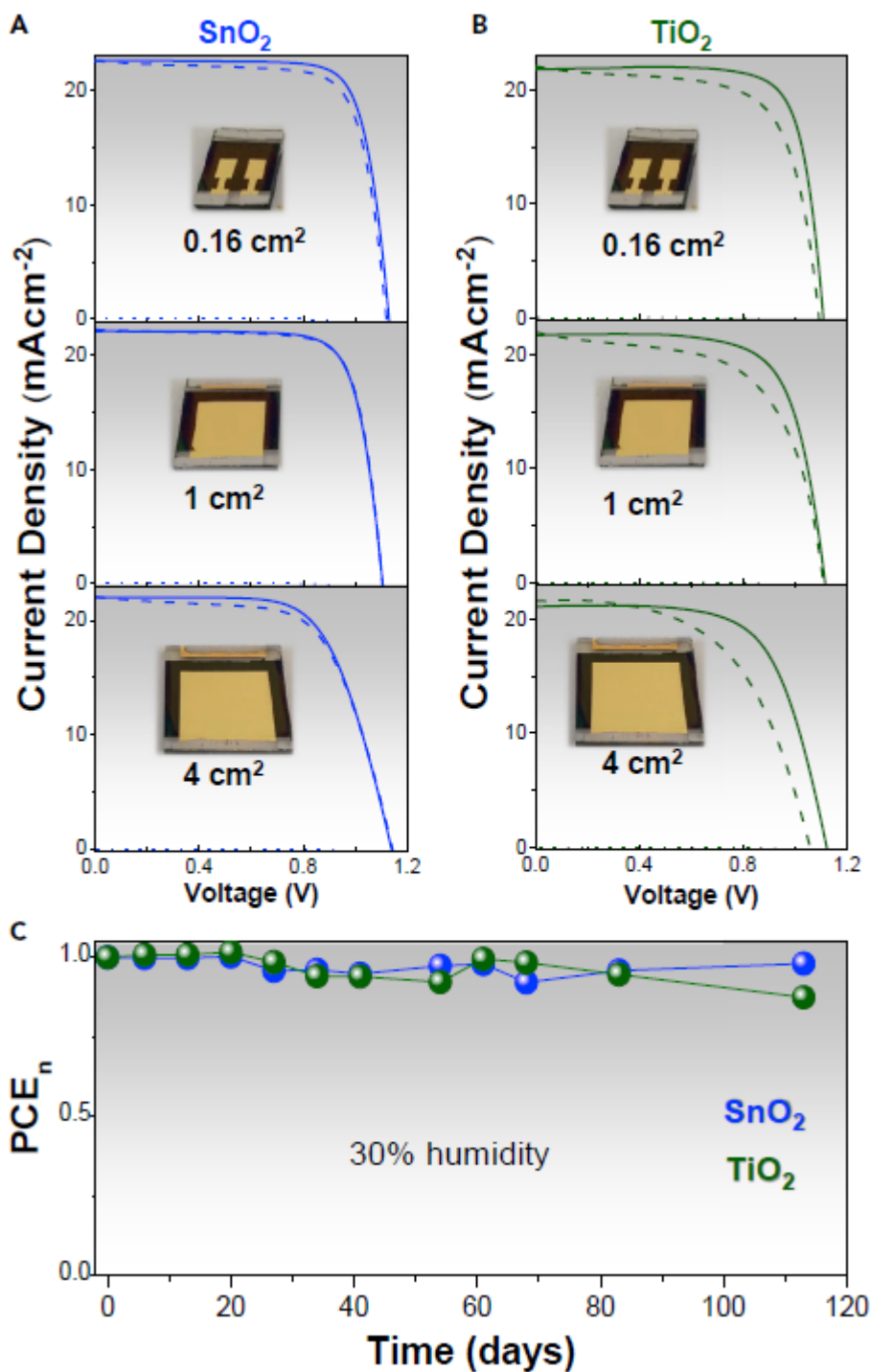
Figure 3: Photovoltaic characteristics of the up-scaled *treated*-MAPbI₃ PSCs. Dark, forward and backward J–V curves of *Treated*-MAPbI₃ PSCs with active areas ranging from 0.16 cm² and 4 cm² (a) based on SnO_2 and on (b) TiO_2 as ETL. Normalized power conversion efficiency (PCE_n) versus time for SnO_2 and TiO_2 based PSCs stored at 30% humidity and measured in air. (see also **Figure S18**, **Figure S19**, **Figure S20**)
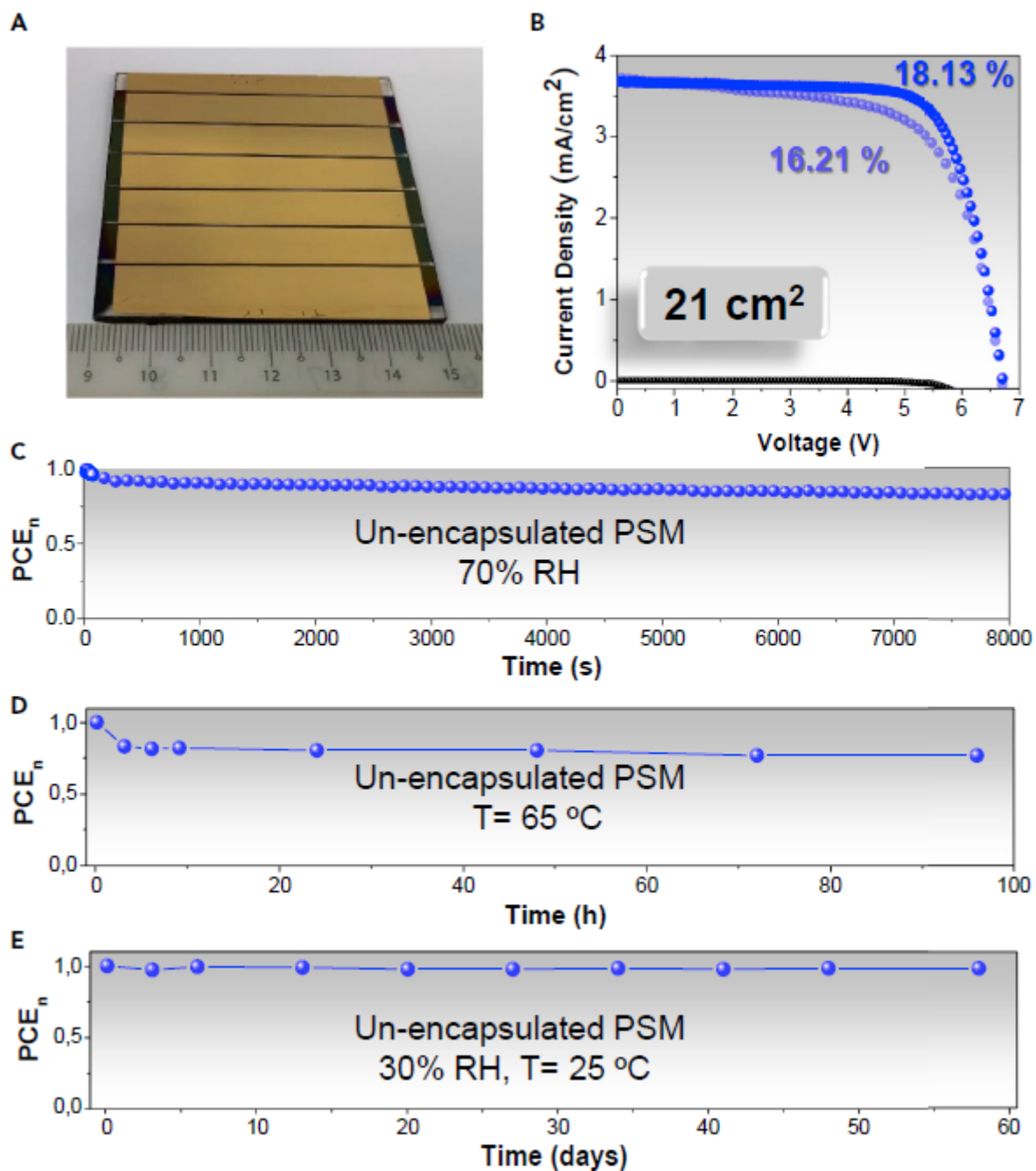
Figure 4: *Treated*-MAPbI$_3$ PSM Photovoltaics Characteristics. (a) Image of a 21 cm^2 active area SnO$_2$ based PSM consisting of series-connected 6 sub cells. (b) *Treated*-MAPbI$_3$ PSM dark, forward and backward J–V curves. (c) Normalized power conversion efficiency (PCE$_n$) versus time under 1 sun continuous illumination at 70% relative humidity measured in air. (d) PCE$_n$ changes at 65 °C over 100 hours in Argon environment and (e) PCE$_n$ over 50 days (shelf-stability). PSM stored in a controlled environment with 35% relative humidity and measures at 70% (RH). The PSM is un-encapsulated for all the measurements.
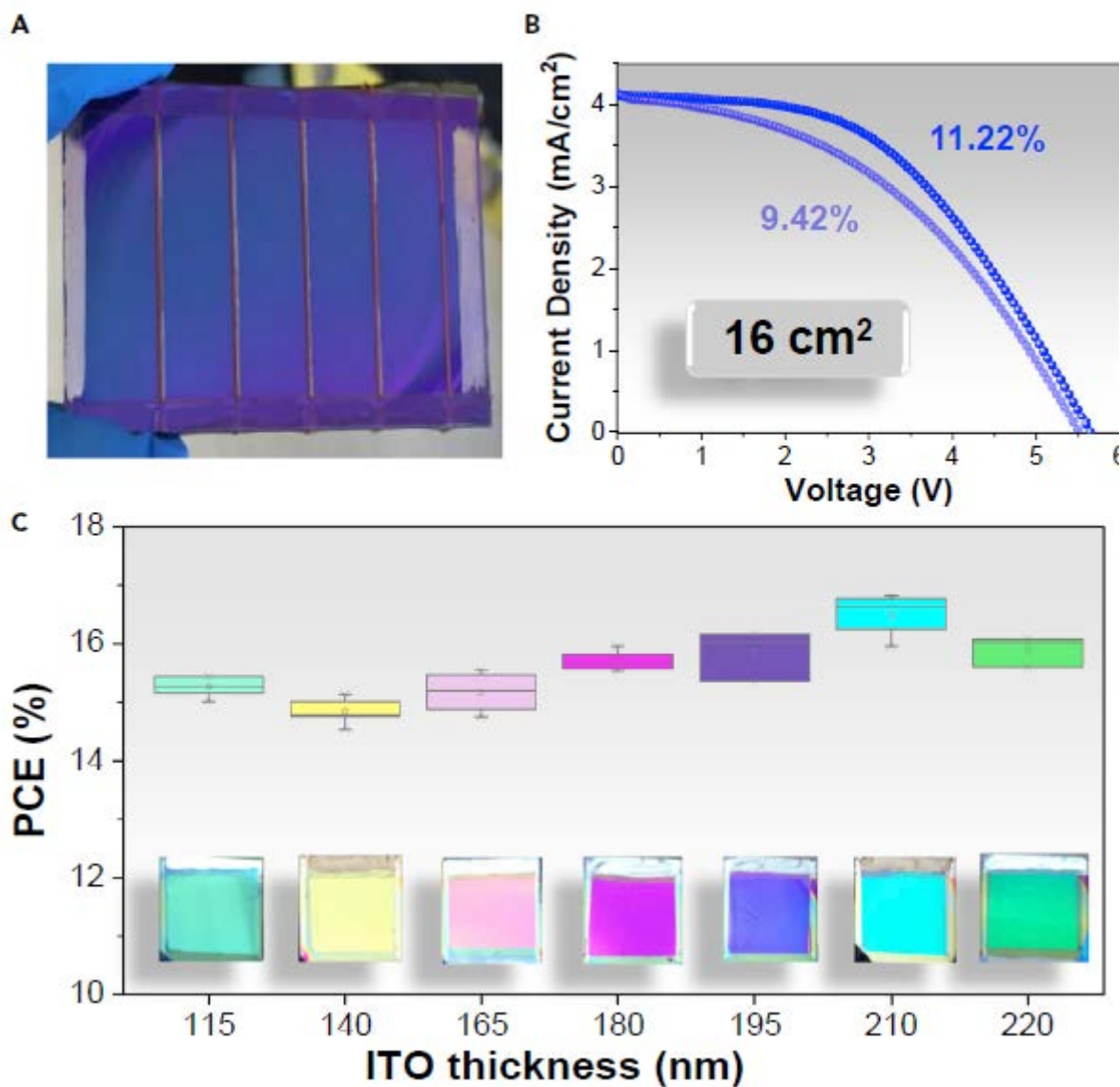
Figure 5: *Treated*-MAPbI$_3$ ST-PSM and ST-PSCs Photovoltaics Characteristics. (a) Image of a 16 cm^2 active area SnO$_2$ based ST-PSM consisting of series-connected 4 sub-cells. (b) ST-PSM dark, forward and backward J–V curves. (c) ST-PSCs' power conversion efficiency as a function of the semi-transparent electrode (ITO) thickness, determining the PSCs color appearance. Photograph of the ST-PSCs in the corresponding position of the ITO thickness. (see also **Figure S21**, **Figure S22**, **Figure S23**, **Figure S24**)
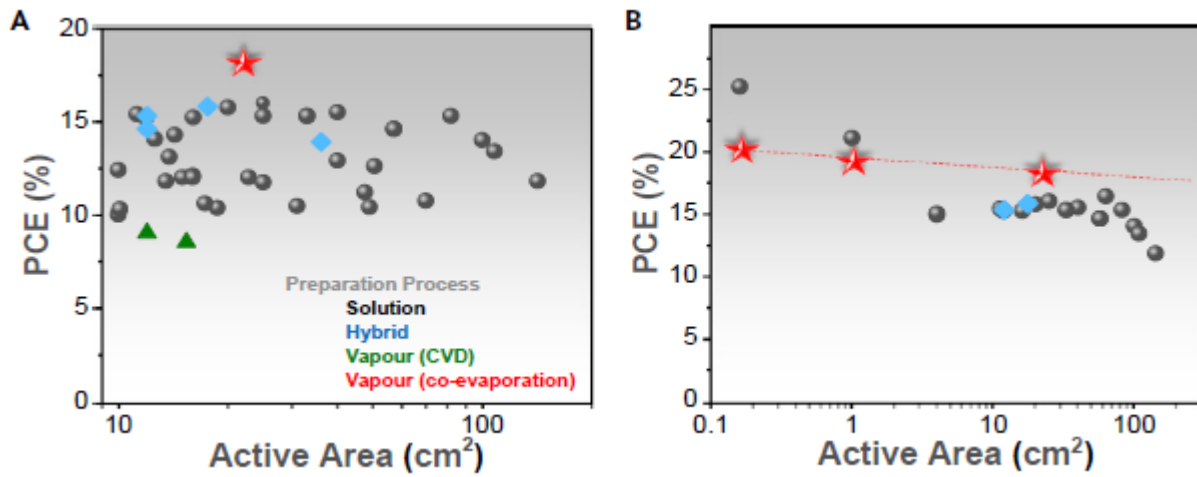
Figure 6: PCE of PSC and PSM versus active areas. (a) Recently reported PCE of PSM with an active area larger 10 cm² fabricated with different preparation methods: solution processes including spin coating, slot die, blade-coating, hot-casting spray-coating, (black spheres); hybrid processes as gas-solid reaction and amine pressure (blue rhomboids) and chemical vapor deposition (green triangles), thermal co-evaporation (red star) (b) PCEs record values for each active area in the range from 1 cm² to 200 cm².

Main Tables and Tables Titles and Legends

Table 2: Small area PSCs Photovoltaic parameters. The J_{sc}, V_{oc}, FF and PCEs values measured in backward scanning mode, of pure MAPbI$_3$, *treated*-MAPbI$_3$, *treated*-MAPbI$_3$+ LiF antireflection coating champion PSCs. The average PCEs (PCE$_{av}$)values have been evaluated over 20 PSCs.

	J_{sc} (mA/cm^2)	V_{oc} (V)	*FF*	PCE (%)	PCE$_{av}$ (%)
MAPbI$_3$	22.3	1.12	76.6	19.13	18.8
Treated-MAPbI$_3$	22.6	1.13	78.0	19.91	19.3
Treated-MAPbI$_3$ + LiF ARC	23.3	1.12	77.7	20.28	19.9

Table 3: Photovoltaic parameters of PSCs with active areas ranging from 0.16 to 4 cm^2. The J_{sc}, V_{oc}, FF and PCEs values, measured in backward scanning mode, are reported for *treated*-MAPbI$_3$ champion PSCs based on SnO$_2$ and TiO$_2$ ETLs.

ETL	Area (cm^2)	J_{sc} (mAcm^2)	V_{oc} (V)	FF (%)	PCE (%)
SnO$_2$	0.16	22.6	1.13	77.98	19.91
	1	22.2	1.12	76.32	18.97
	4	22.0	1.14	66.11	16.59
TiO$_2$	0.16	21.8	1.11	77.51	18.75
	1	21.7	1.11	71.10	17.12
	4	21.1	1.12	65.93	15.58

Table 4: Photovoltaic parameters of PSM with 21 cm^2 active area. The J_{sc}, V_{oc}, FF and PCE values of a *treated*-MAPbI$_3$ PSM based on SnO$_2$ are reported for both backward and forward scanning mode.

Area (cm^2)	Scan direction	V_{oc} (V)	J_{sc} (mA/cm^2)	*FF* (%)	PCE (%)	PCE$_{mean}$ (%)
21	Back	6.71	3.68	73.44	18.13	17.17%
	Forward	6.69	3.72	65.06	16.21	

Table 5: Colourful ST-PSCs photovoltaic parameters and CIE coordinates. The J_{sc}, V_{oc}, FF, and PCEs values of colorful *treated*-MAPbI$_3$ ST-PSCs are reported as a function of the ITO thickness together with the correspondent CIE coordinates.

ITO thickness (nm)	V_{oc} (V)	J_{sc} (mA/cm^2)	FF (%)	PCE (%)	CIE
115	0.988	21.14	73.95	**15.44**	(0.32, 0.40)
140	0.990	21.65	70.67	**15.14**	(0.39, 0.46)
165	0.972	21.53	74.32	**15.56**	(0.42, 0.33)
180	0.988	22.53	71.65	**15.96**	(0.34, 0.21)
195	0.963	22.32	75.22	**16.17**	(0.24, 0.19)
210	1.000	21.89	76.84	**16.83**	(0.21, 0.38)
220	0.990	22.13	73.38	**16.09**	(0.24, 0.45)

Table S1: PSM with active area larger than 10 cm^2. Power conversion efficiencies together with the active layer composition, the deposition methods, the module' active area are reported.

No.	Active Layer	Deposition Methods	Active Area (cm^2)	Power Conversion Efficiency (%)[1]	Ref
1	$K_xCs_{0.05}(FA_{0.85}MA_{0.15})_{0.95}Pb(I_{0.85}Br_{0.15})_3$	spin coating with antisolvent	20	15.76	[1]
2	$CH_3NH_3PbI_{3-x}Cl_x$	one-step spin coating	4	14.9	[2]
3	$CH_3NH_3PbI_{3-x}Cl_x$	Blade coating	12.6	14.06	[3]
4	$CH_3NH_3PbI_{3-x}Cl_x$	Hot casting	15	12.0	[4]
5	$CH_3NH_3PbI_3$	one-step spin coating	10	10.0	[5]
6	$CH_3NH_3PbI_3$	one-step spin coating	40	12.9	[6]
7	$CH_3NH_3PbI_3$	double-step method (spin coating of PbI_2 + dipping in CH_3NH_3I solution)	50.56	12.6	[7]
8	$Cs_{0.06}MA_{0.27}FA_{0.67}PbI_{2.7}Br_{0.3}$	two-step coating (PbI_2/CsI + MAI/FAI/MABr/MACl)	22.8	12	[8]
9	$CH_3NH_3PbI_3$	two-step spin coating	11.25	15.4	[9]
10	$CH_3NH_3PbI_3$	conversion of amine complex precursors with a pressure step	17.6 / 36.1	15.8 / 13.9	[10]
11	$CH_3NH_3PbI_3$	gas−solid reaction of $HPbI_3(Cl)$ (by spin coating) and CH_3NH_2 gas	12.0	15.3	[11]
12	$Cs_{0.07}FA_{0.93}PbI_3$	spin-coated $PbI_2 \cdot DMSO$ and CVD deposition of FAI	12.0	14.6	[12]
13	$CH_3NH_3PbI_3$	CVD	15.4	8.5	[13]
	FAPbI3		12	9.0	
14	$(HOOC(CH_2)_4NH_3)_2PbI_4/CH_3NH_3PbI_3$	drop casting	47.6	11.2	[14]
15	$CH_3NH_3PbI_{3-x}Cl_x$	sheet-to-sheet slot die coating	142	11.8	[15]
16	$CH_3NH_3PbI_3$	Blade coating	33 / 57.2	15.3 / 14.6	[16]
17	$CH_3NH_3PbI_{3-x}Cl_x$	spray-coating	40	15.5	[17]
18	$(FAPbI_3)0.95(MAPbBr_3)_{0.05}$	two consecutive spin-coating steps	24.97	16.0	[18]
19	$[CsPbI_3]_{0.05}[(FAPbI_3)_{0.85}(MAPbBr_3)_{0.15}]_{0.95}$	spin coating with antisolvent	25 / 100	15.3 / 14.0	[19]
20	$[CsPbI_3]_{0.05}[(FAPbI_3)_{0.85}(MAPbBr_3)_{0.15}]_{0.95}$	spin coating with antisolvent	82 / 108	15.3 / 13.4	[20]
21	$Cs_{0.05}(FA_{0.85}MA_{0.15})_{0.95}Pb(I_{0.85}Br_{0.15})_3$	spin coating with	16.07	15.22	[21]

---

[1] Here we summarize only the active area efficiency.

		antisolvent			
22	$MA_{0.7}FA_{0.3}PbI_3$	blade coating	18.7	10.36	[22]
23	$(HC(NH_2)_2PbI_3)_{0.85}(CH_3NH_3PbBr_3)_{0.15}$	antisolvent spraying	16	12.1	[23]
24	$(Semi\text{-}T)Cs_{0.1}FA_{0.9}PbI_{2.865}Br_{0.135}$	anti-solvent method	16	12.0	[24]
25	$CH_3NH_3PbI_3$	anti-solvent method	13.8	13.1	[25]
			11.9	15.2	
26	$(5\text{-}AVA)x(MA)1\text{-}xPbI3$ [carbon]	drop casting	49	10.4	[26]
27	$CH_3NH_3PbI_3$	Blade coating of PbI_2, Dipping MAI	10.1	10.3	[27]
28	$CH_3NH_3PbI_3$	anti-solvent method	13.5	11.8	[28]
29	$K_xCs_{0.05}(FA_{0.85}MA_{0.15})_{0.95}Pb(I_{0.85}Br_{0.15})_3$	spin coating with antisolvent	10	12.40	[29]
30	$(5\text{-}AVA)x(MA)1\text{-}xPbI3$ [carbon]	drop casting	31	10.46	[30]
			70	10.74	
31	[carbon]$CH_3NH_3PbI_3$	Slot-die coating + gas-pumping	17.3	10.6	[31]
32	$[CsPbI_3]_{0.05}[(FAPbI_3)_{0.85}(MAPbBr_3)_{0.15}]_{0.95}$	spin coating with antisolvent	25	11.73	[32]
33	$FA_{0.85}MA_{0.15}Pb(I_{0.85}Br_{0.15})_3$	spin coating with antisolvent	14.3	14.28	[33]
34	$MAPbI_3$	blade coating	63.7	16.4	[34]
35	$MAPbI_3$	surfactant-assisted blade-coating	33.0	15.3	[35]
			57.2	14.6	
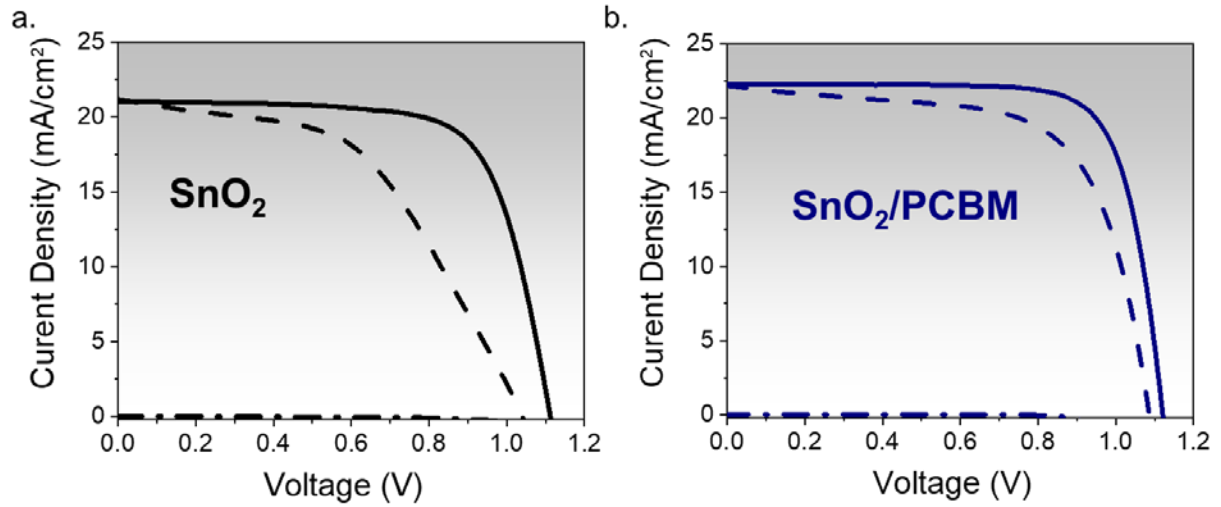
Figure S1. Pristine thermally evaporated MAPbI₃ PSCs with SnO₂ as HTL. J-V curves of SnO$_2$(a) and SnO$_2$/PCBM (b) measured in the backward scan and forward scan.

Table S2. Photovoltaic parameters of PSCs based on SnO$_2$ and SnO$_2$/PCBM. The V_{oc}, J_{sc} FF and PCEs values are reported for both backward and forward scans.

ETL	Scan	V_{oc} (V)	J_{sc} (mA/cm^2)	FF (%)	Efficiency (%)	Hysteresis index
SnO$_2$	Backward	1.11	21.1	71.1	**16.6**	**0.594**
	Forward	1.04	21.2	50.2	**11.1**	
SnO$_2$/PCBM	Backward	1.12	22.3	76.6	**19.1**	**0.137**
	Forward	1.08	22.2	65.4	**16.7**	
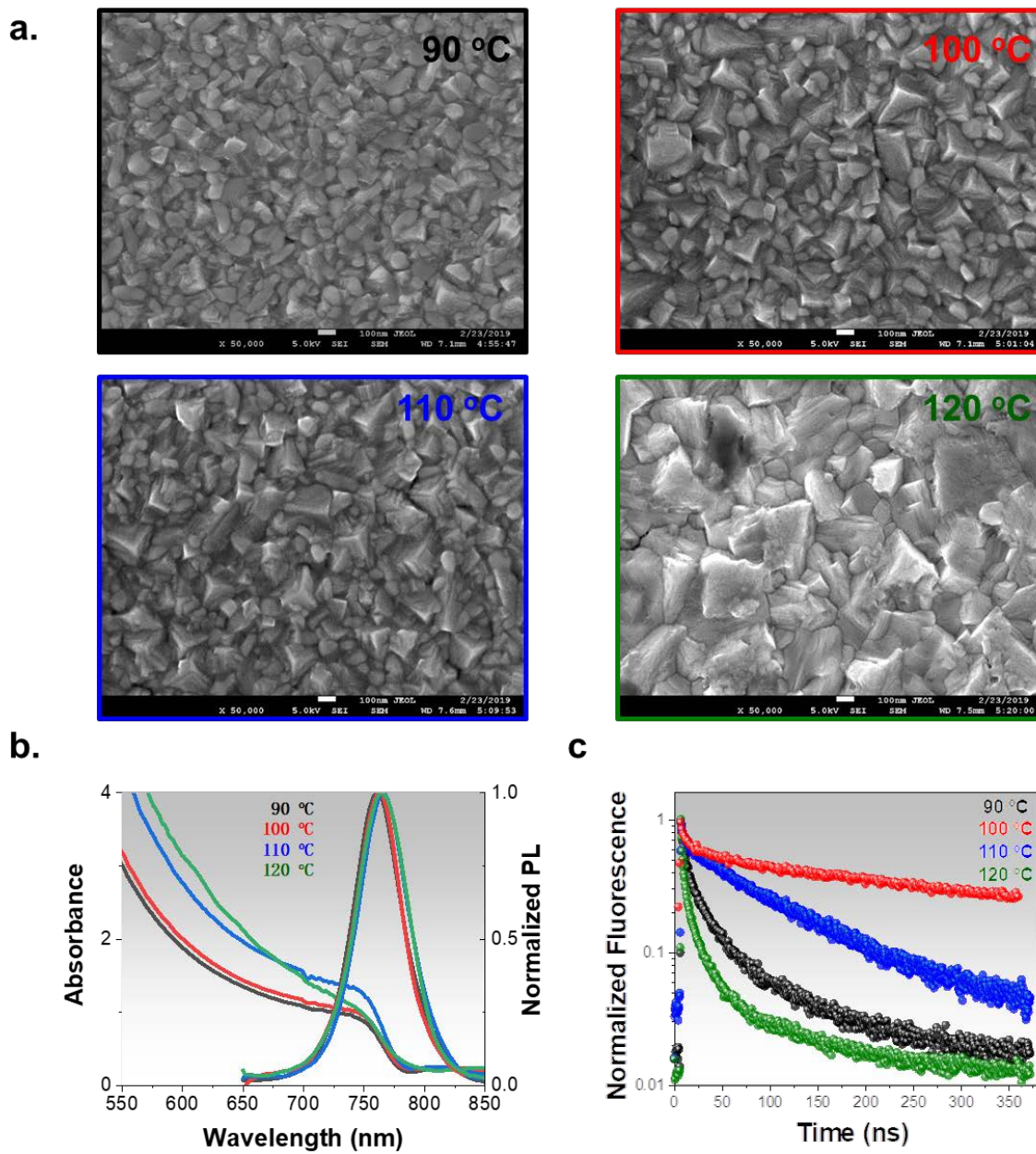
Figure S2. MAPbI₃ thin films grown at different MAI temperature (90 ºC, 100 ºC, 110 ºC, 120 ºC): a) Film morphology: SEM top view. b) Absorption and photoluminescence emission spectra. c) time-resolved photoluminescence decays.
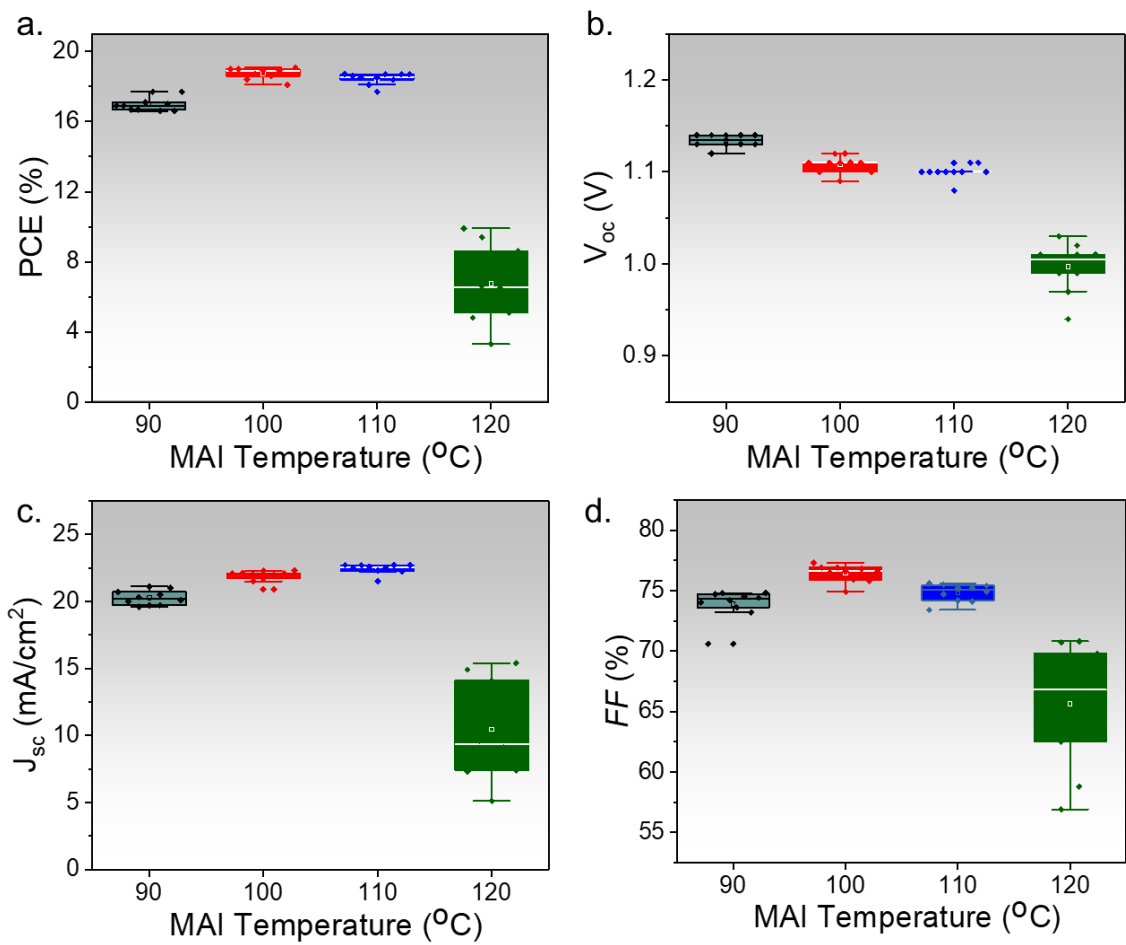
Figure S3. MAPbI₃ PSCs photovoltaics statistics using MAPbI₃ thin films grown at different MAI temperatures (90 ºC, 100 ºC, 110 ºC, and 120 ºC) a) Power conversion efficiency, b) V_{oc}, c) J_{sc} and d) FF.
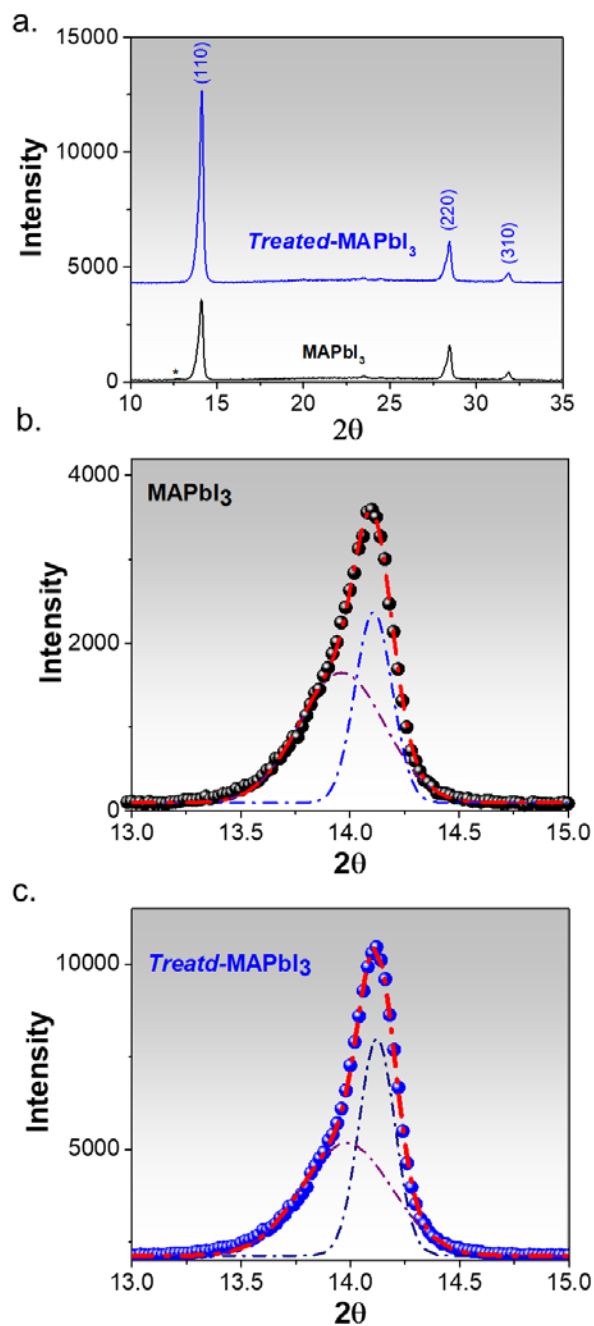
Figure S4. **X-ray patterns of MAPbI$_3$ and** *treated*–**MAPbI$_3$**. a) X-ray spectrograph in the range 10- 35°. A zoom of the peak at (110) at 14.1° of and Gaussian fitting curves of MAPbI$_3$ and *treated*–MAPbI$_3$ are reported in b) and c) respectively. According to Scherrer equation: d=(0.89*λ)/(FWHM*cosθ) where λ is the wavelength of X-ray, FWHM is full-with-at-half-maximum of the diffraction peak, θ is the diffraction angle. The full width at half maximum of peak (110) at 14.1°, evaluated by a Gaussian fitting, are 0.170 ± 0.002 and 0.165± 0.001 for perovskite before and after post-treatment, resulting in the calculated crystal size being 82.1± 0.2 nm and 86.1 ± 0.1 nm, respectively.
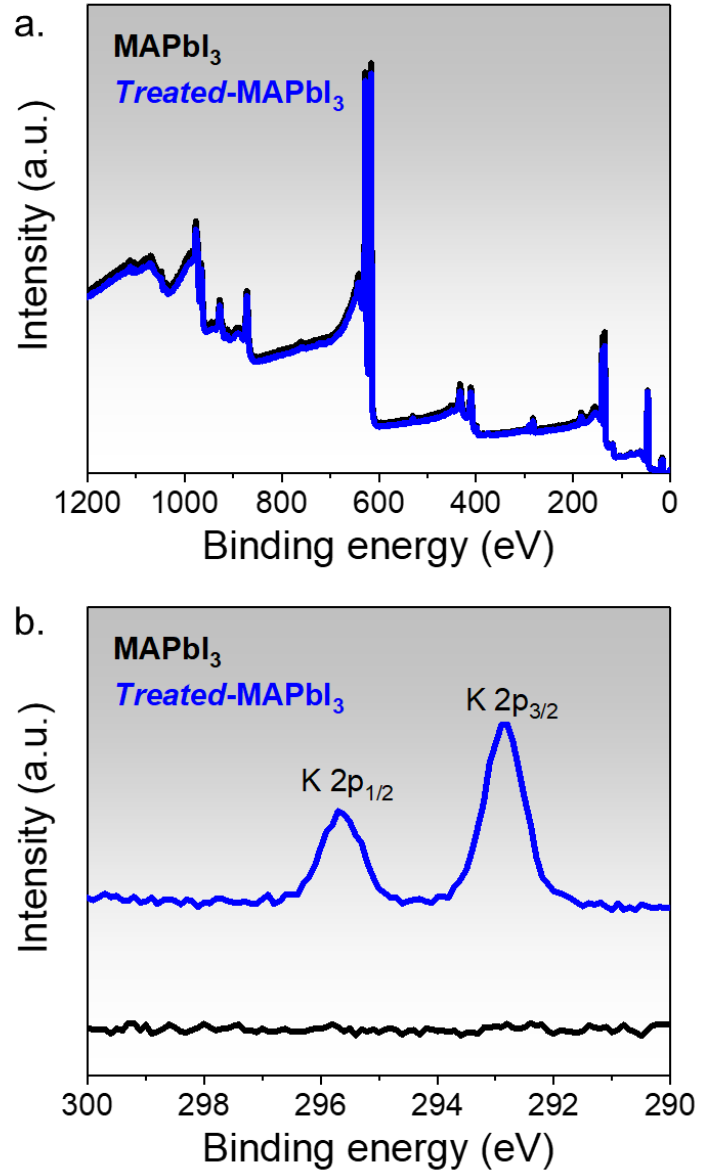
Figure S5: XPS spectra of MAPbI₃ and *treated*–MAPbI₃. a) The full spectra in the region between 0 to 1200 eV and b) a zoom between 300 and 290 eV where it is possible to observe the K 2p orbital peaks in the *treated*-MAPbI₃ films.
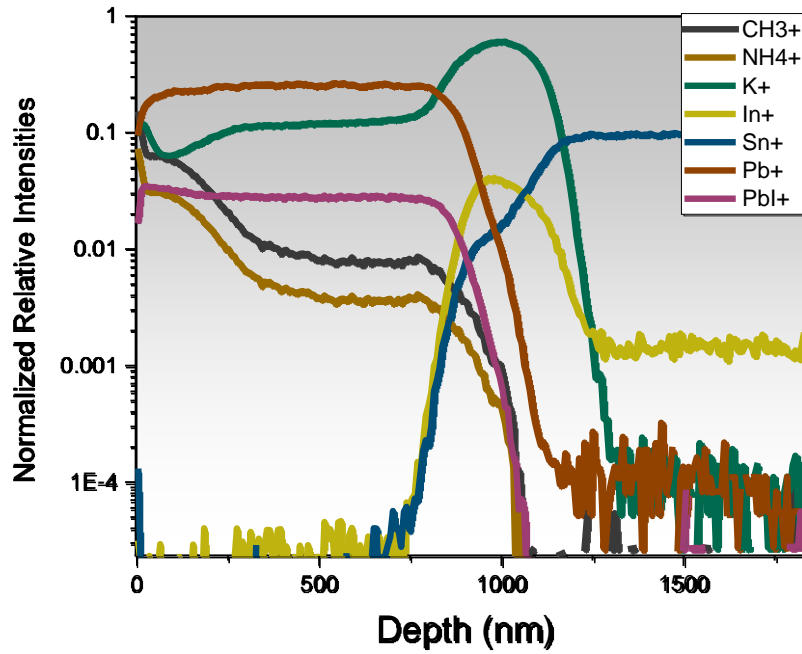
Figure S6. time-of-flight secondary ion mass spectroscopy (TOF-SIMS) of *treated*-MAPbI₃ thin-film. The depth profile for the positive ions (CH3⁺, NH4⁺, K⁺, In⁺, Sn⁺, Pb⁺, PbI⁺) in a) on a *treated*-MAPbI₃ film deposited on PCBM/SnO₂/FTO glass substrate.
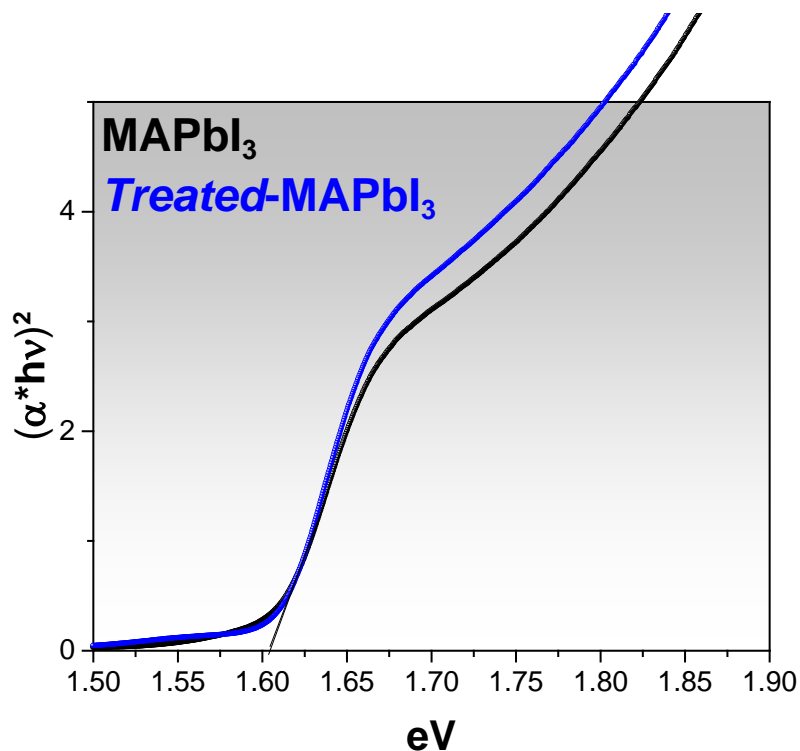
Figure S7. *Tauc*-plot. The pristine thermally evaporated MAPbI$_3$ film (black line) and *treated*-MAPbI$_3$ (blue line) film *tauc* curves confirmed a consistent bandgap of 1.61 eV.

Table S3. TRPL fitting parameters of MAPbI$_3$ and *treated*-MAPbI$_3$. TRPL decay curves of the MAPbI$_3$ and *treated*-MAPbI$_3$ thin-films, shown in **Figure 1c,** have been fitted with a double exponential function. The characteristics decay times (t$_1$ and t$_2$), their relative weight (A$_1$ and A$_2$) are reported together with the average fluorescence lifetime calculated as $\tau_{av} = (\tau_{1*}A_1 + \tau_{2*}A_2)/(A_1 + A_2)$.

Sample	A$_1$(%)	t$_1$(ns)	A$_2$(%)	t$_2$(ns)	t$_{av}$ (ns)
MAPbI$_3$	12	31	88	410	364 ±5
treated-MAPbI$_3$	48	42	52	293	172 ±5
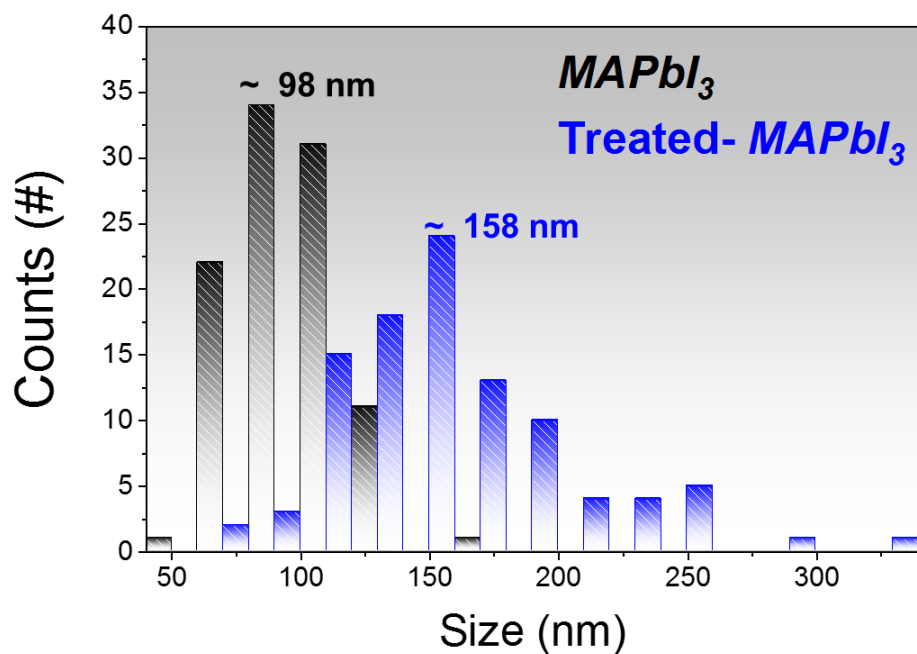
Figure S8. The grain size distribution of the MAPbI₃ and *treated*-MAPbI₃ films. The grain sizes have

been evaluated from the top-view SEM images, **Figure 1c,** over 100 grains using ImageJ software.

a.

b.
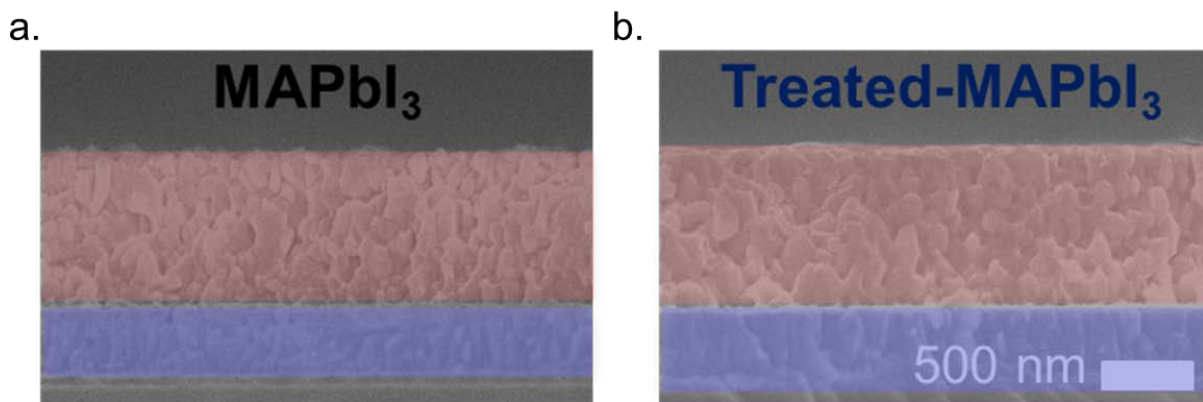
Figure S9. Cross-sectional SEM images of the MAPbI₃ and *treated*-MAPbI₃ films. The films have

been deposited on FTO/ glass substrate.
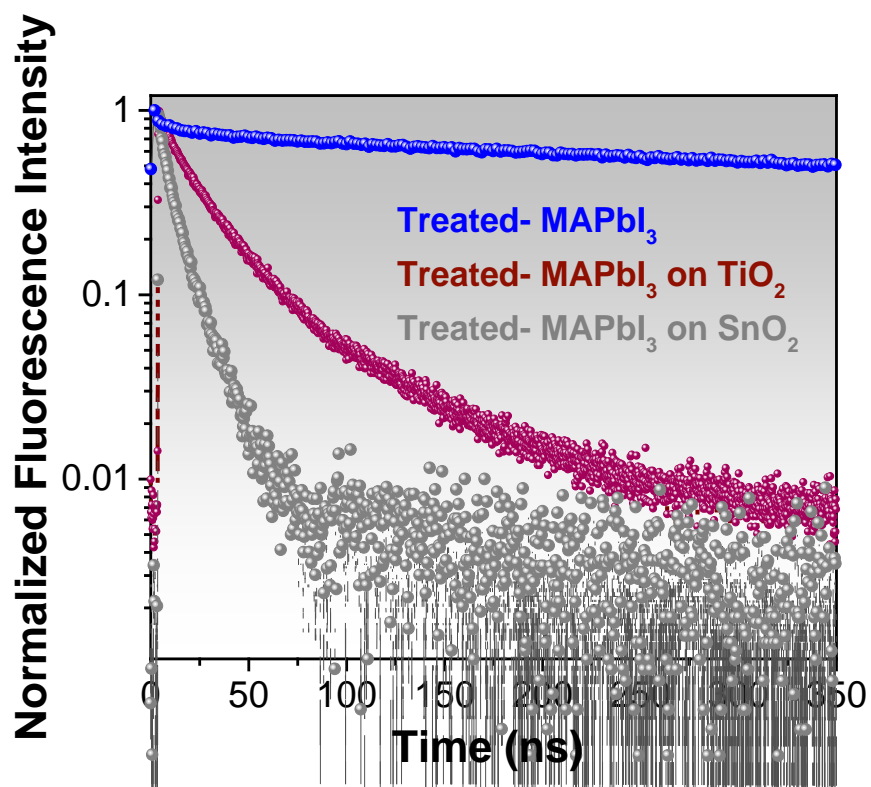
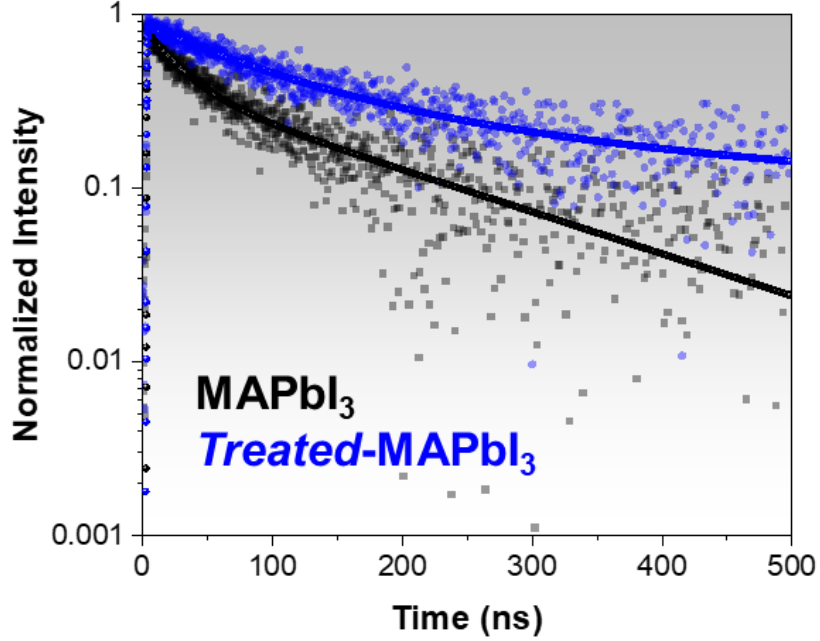**Figure S10. TRPL quenching.** TRPL decay curves of *treated*-MAPbI$_3$ films on PCBM/SnO$_2$/ FTO/glass and PCBM/TiO$_2$/FTO/glass substrates.

Figure S11: Photobleaching of MAPbI₃ and *treated*-MAPbI₃ films. The decay curves of MAPbI₃ (black line) and *treated*-MAPbI₃ (blue line) are reported together with their double exponential fitting curves.

Table S4. MAPbI₃ and *treated*-MAPbI₃ TA photo-bleaching peak fitting parameters. Double exponential fitting parameters of the TA photo-bleaching peak of the MAPbI₃ and *treated*-MAPbI₃ reported **Figure S11**. The characteristics decay times (t_1 and t_2), relative weight (A_1 and A_2) are reported together with the average fluorescence lifetime calculated as $\tau_{av} = (\tau_{1*}A_1 + \tau_{2*}A_2)/(A_1 + A_2)$.

Sample	A₁(%)	t₁(ns)	A₂(%)	t₂(ns)	t_av (ns)
MAPbI₃	52.1	27 ± 2	47.9	180 ± 9	100 ± 4
treated-MAPbI₃	70.3	104 ± 10	29.7	820 ± 40	320 ± 20
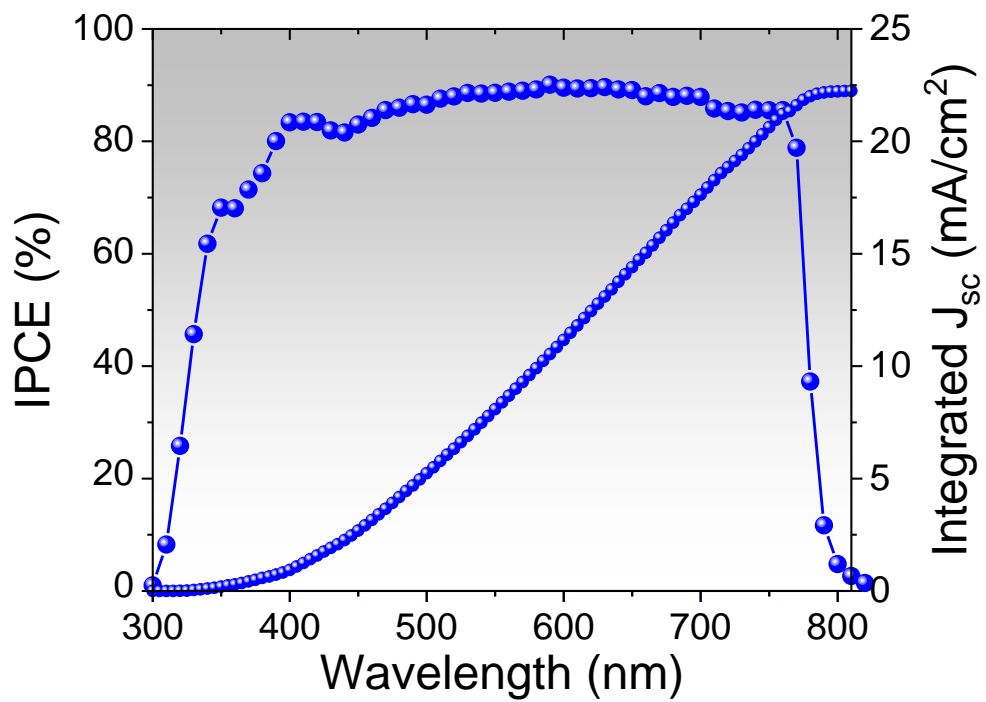
Figure S12: *treated*-**MAPbI₃ PSC IPCE spectra**. On the right axes, the integrated J_{sc} calculated from the
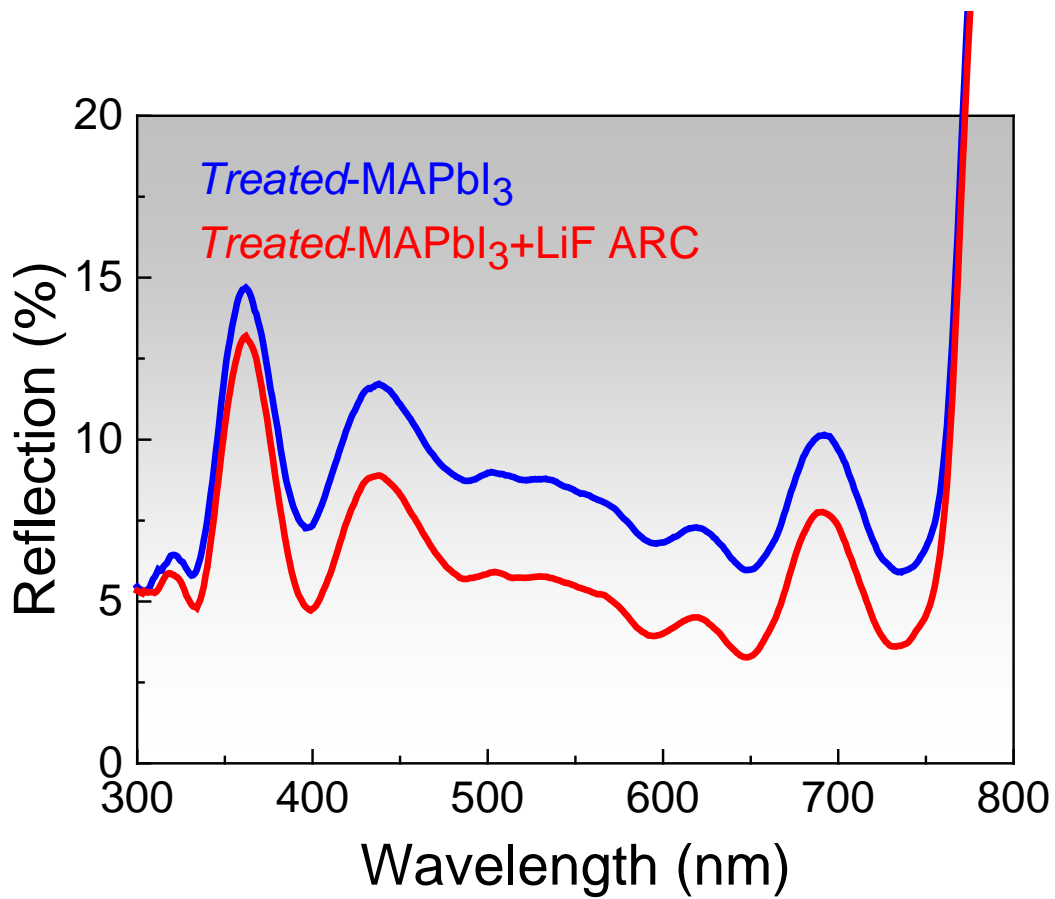
IPCE spectra is reported.

Figure S13: Reflectance spectra. The reflectance spectra in the UV visible region from 300 yo 800 nm is reported for *treated*-MAPbI$_3$ (blue) and *treated*-MAPbI$_3$+ARC (red) PSCs.
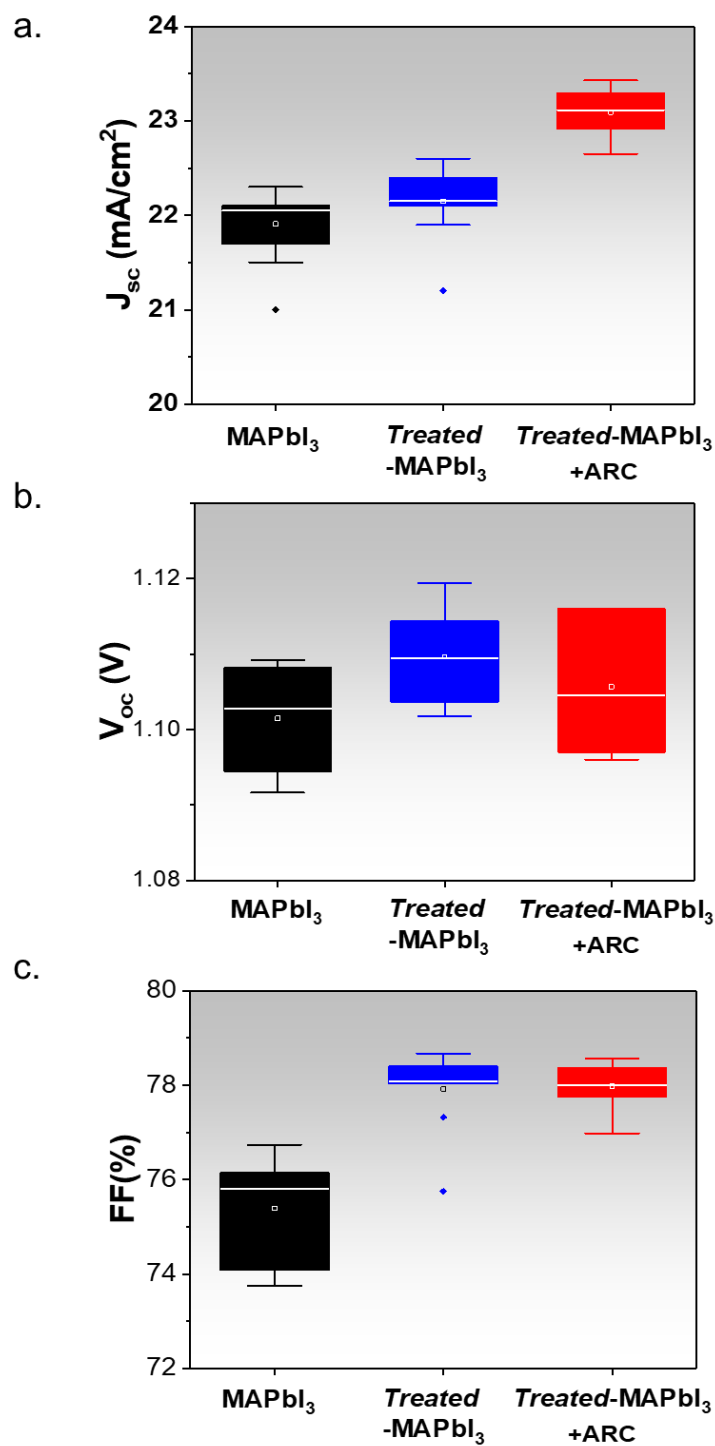
Figure S14: Small area PSCs photovoltaics statistics. Photovoltaic parameters statistical distributions of a) V_{oc}, b) J_{sc} and c) *FF* of PSCs with pristine thermal evaporated MAPbI$_3$ (black), *treated*-MAPbI$_3$ (blue) and *treated*-MAPbI$_3$ + together with LiF as anti-reflection coating (ARC) (red).
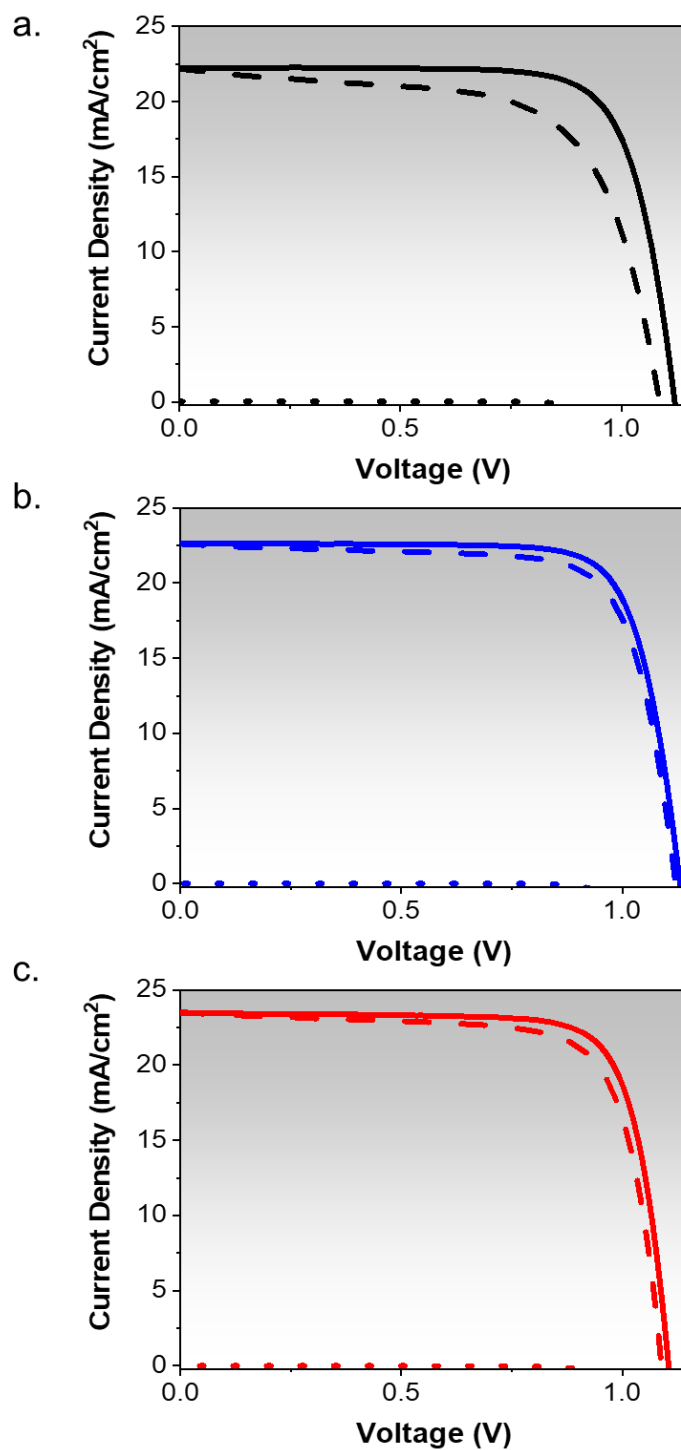
Figure S15: J-V curves of MAPbI₃ (black), *treated***-MAPbI₃ (blue) and** *treated***-MAPbI₃ +ARC PSCs (red).** The J-V curves of representative PSCs are reported for both backward scan (solid line) and forward scan (dash line).

Table S5: Small area photovoltaic parameters of MAPbI₃, *treated*-MAPbI₃ and *treated*-MAPbI₃+ARC PSCs. The V_{oc}, J_{sc} FF and PCEs values are reported for both backward and forward scans together with PCE_{mean} and hysteresis index.

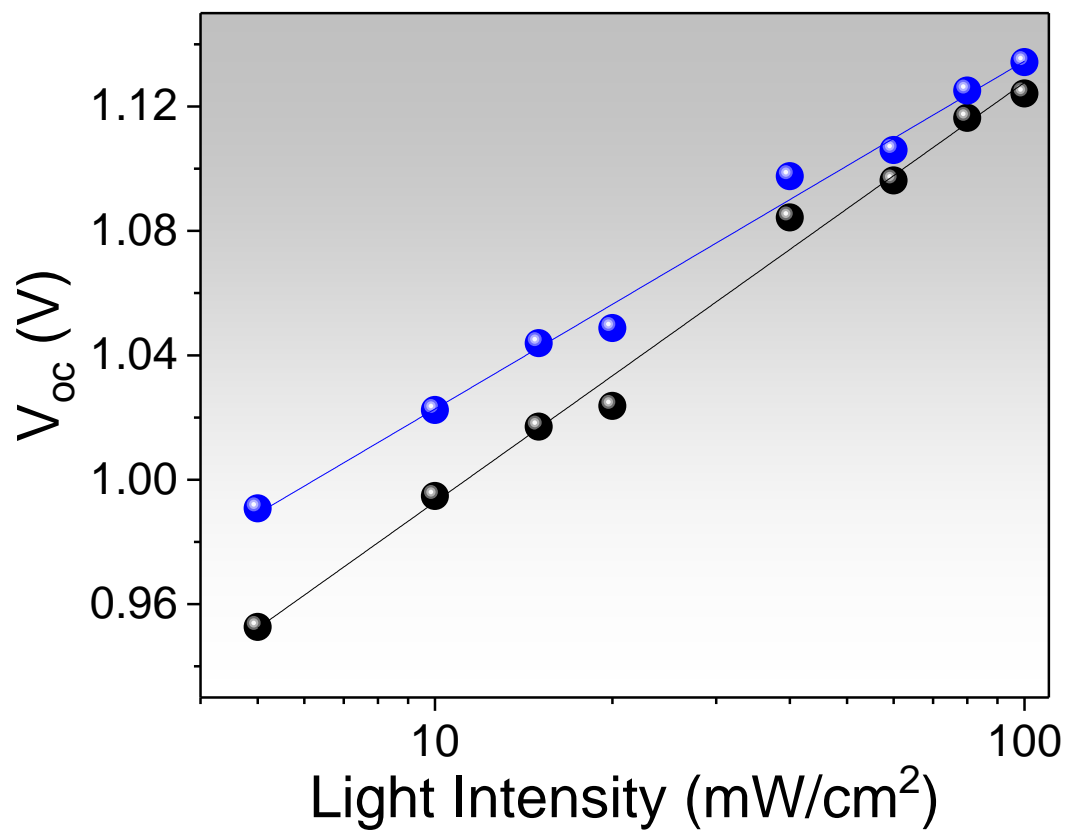|	Scan Direction	J_{sc} (mA/cm²)	V_{oc} (V)	FF (%)	PCE (%)	PCE_{mean} (%)	Hysterisis index
MAPbI₃	Backward	22.3	1.12	76.6	19.13	17.43	0.137
	Forward	22.2	1.08	65.4	15.73		
treated-MAPbI₃	Backward	22.6	1.13	78.0	19.91	19.46	0.040
	Forward	22.6	1.12	75.1	19.01		
treated-MAPbI₃ + ARC	Backward	23.3	1.12	77.7	20.28	19.79	0.031
	Forward	23.4	1.10	75.0	19.30		

Figure S16. V$_{oc}$ trend *vs* light illumination. MAPbI$_3$ (black) and *treated*-MAPbI$_3$ (blue) PSCs Voc trend have been fitted with a linear equation (*a+bx*) from which it has been evaluated a slope (*b*) of 1.95 K$_B$T/q and 1.87 K$_B$T/q respectively.
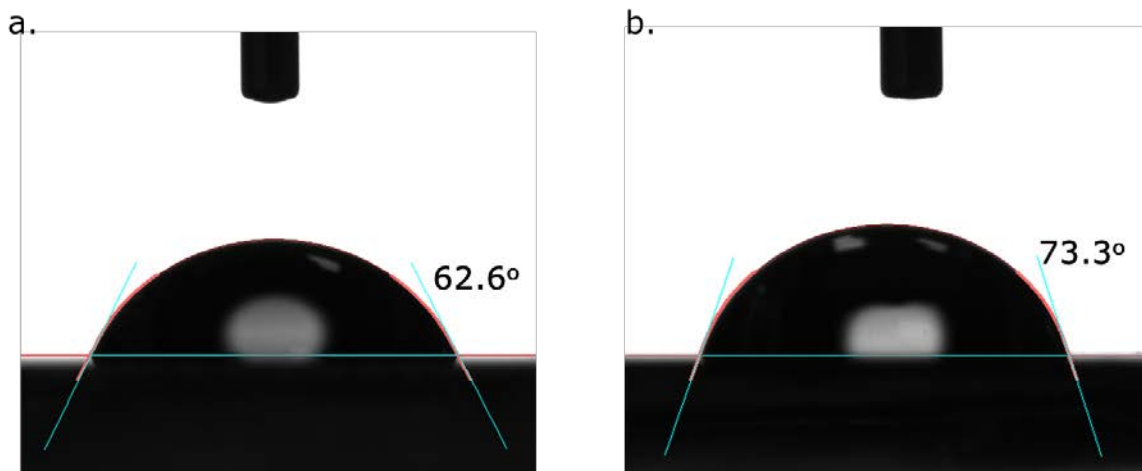
Figure S17. Contact angle measurements. The contact angle of the a) pristine MAPbI$_3$ and b) *treated-*MAPbI$_3$ perovskite film.

Figure S18: Photos of MAPbI₃ perovskite film. The films have been thermally evaporated in the same batch deposited on substrates of different sizes.
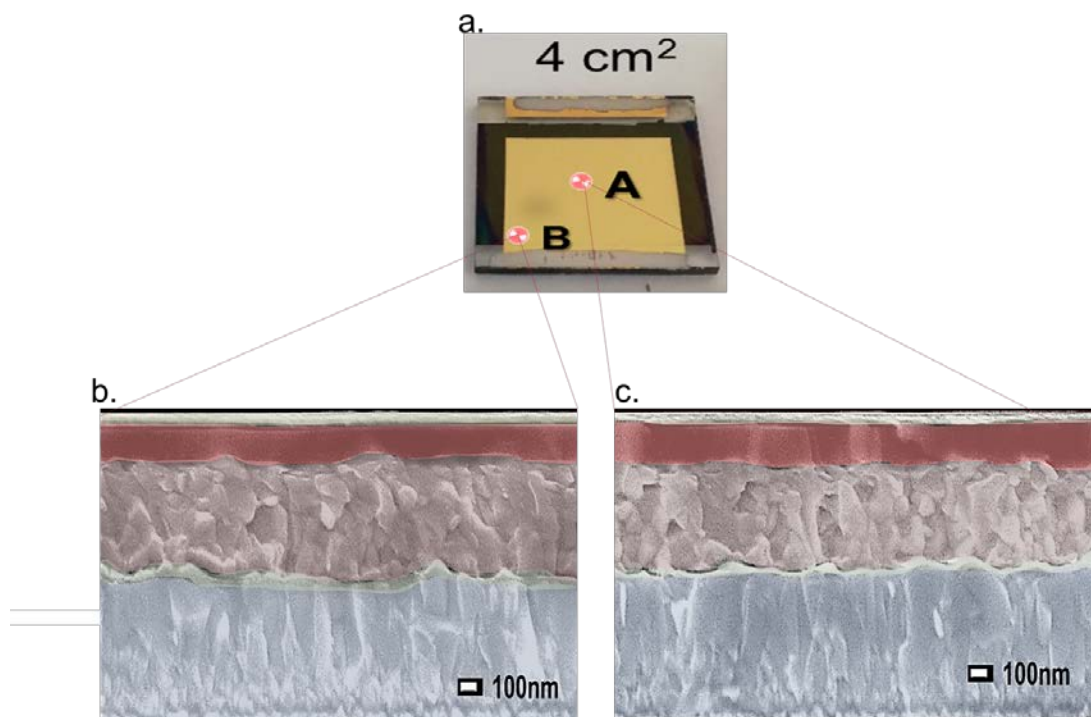
Figure S19: Large area MAPbI$_3$ PSC on Glass/FTO/SnO$_2$ substrate. a) 4 cm^2 PSC photograph. Cross-sectional SEM images of b) point A and c) point b, respectively.
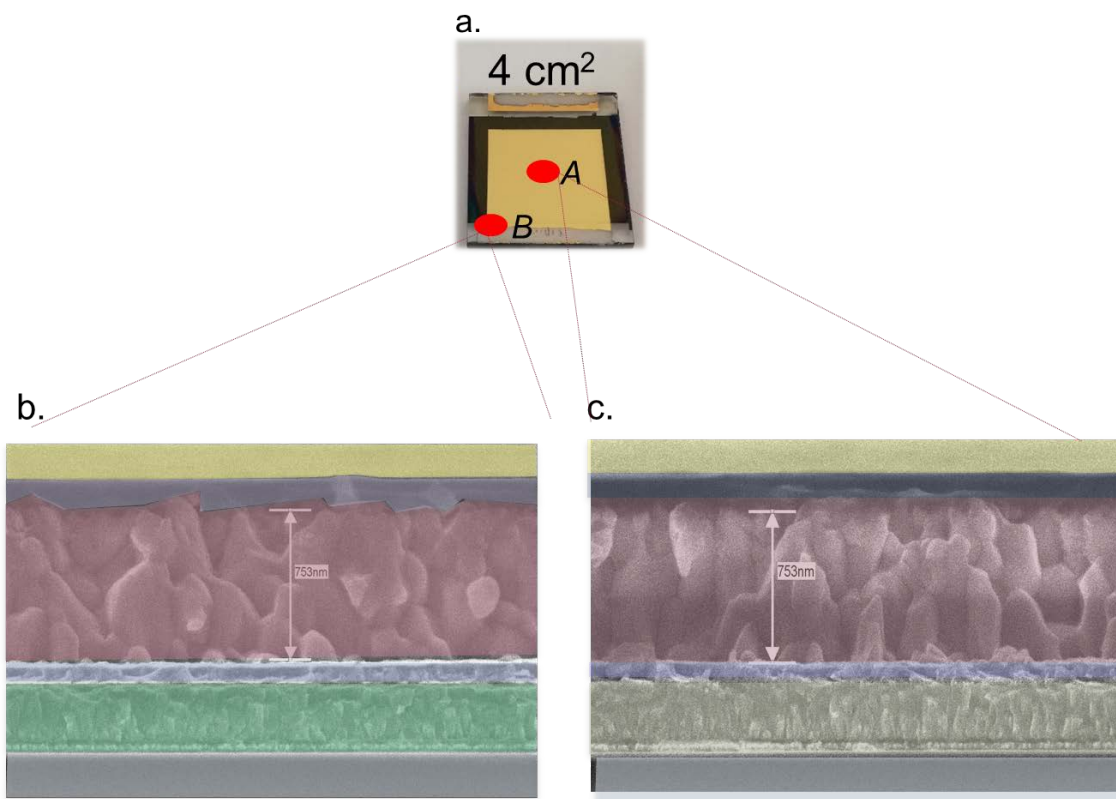
Figure S20: Large area MAPbI₃ PSC on Glass/FTO/TiO₂ substrate. a) 4 cm² PSC photograph. Cross-sectional SEM images of b) point A and c) point b, respectively.
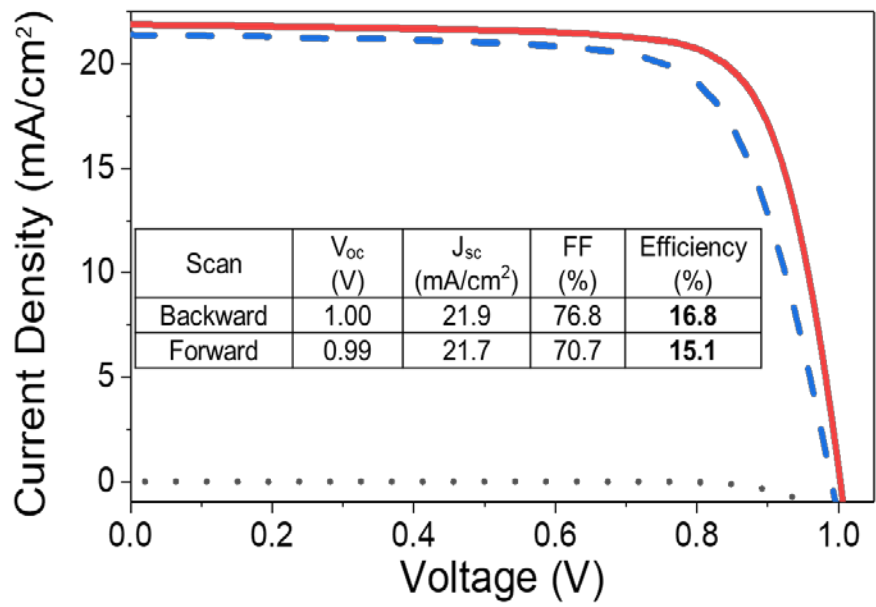
Scan	V_{oc} (V)	J_{sc} (mA/cm^2)	FF (%)	Efficiency (%)
Backward	1.00	21.9	76.8	**16.8**
Forward	0.99	21.7	70.7	**15.1**

Figure S21: J-V curves of the champion semitransparent *treated*-MAPbI₃. The J-V curves have been measured both in the backward scan (solid line) and forward scan (dash line).
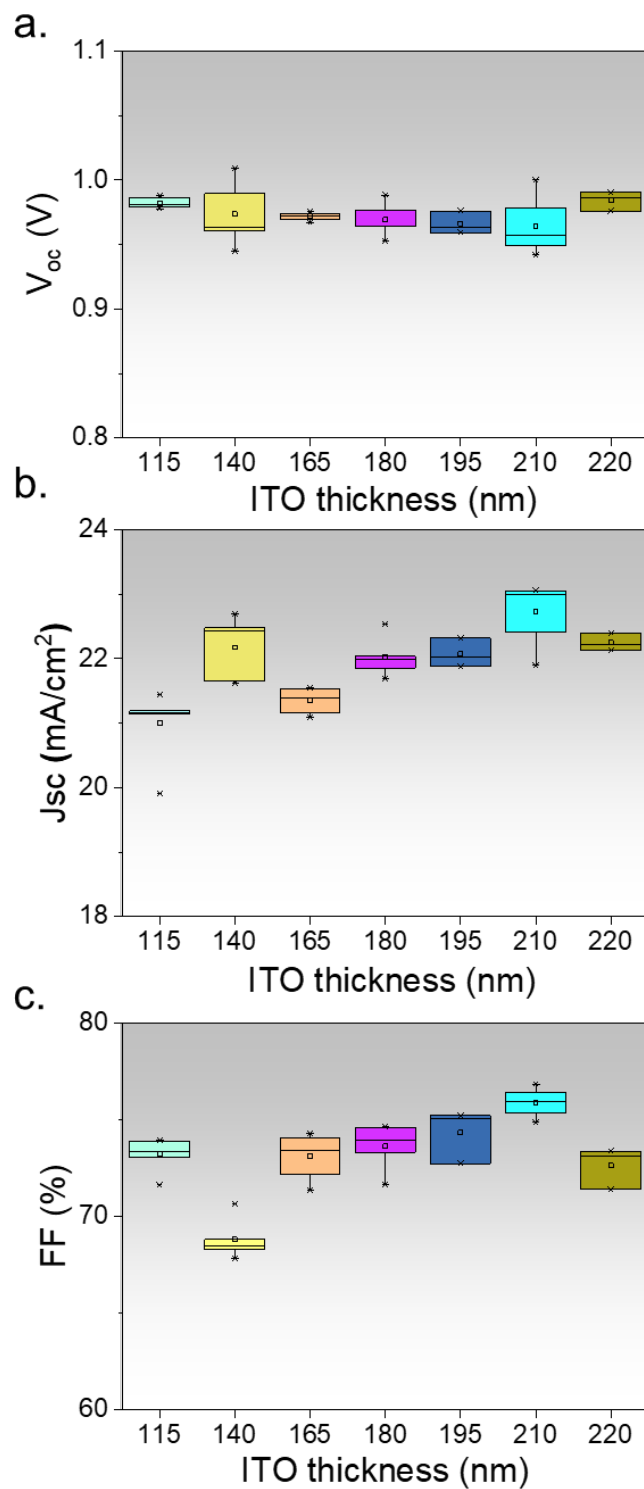
Figure S22: Photovoltaic parameters statistical distributions of semi-transparent PSCs. a) V_{oc}, b) J_{sc} and c) *FF* of solar cells with different ITO thickness from 115 nm to 220 nm.
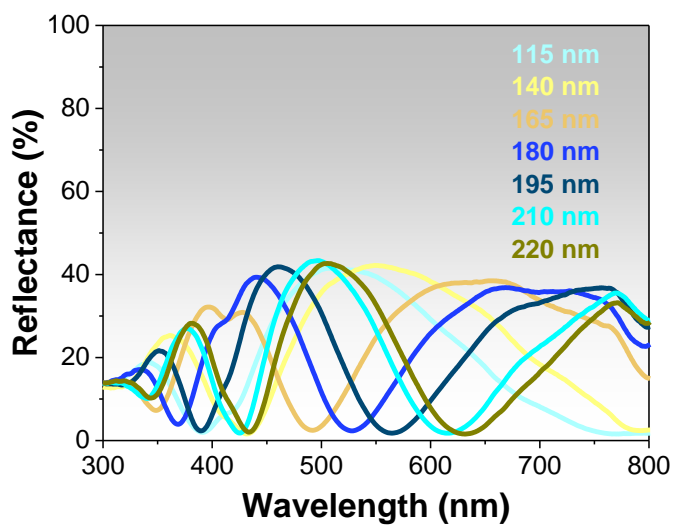
Figure S23: ST-PSCs Light reflectance spectra. The UV-visible reflectance spectra are reported for PSCs with ITO thickness ranging from 115 to 220 nm.
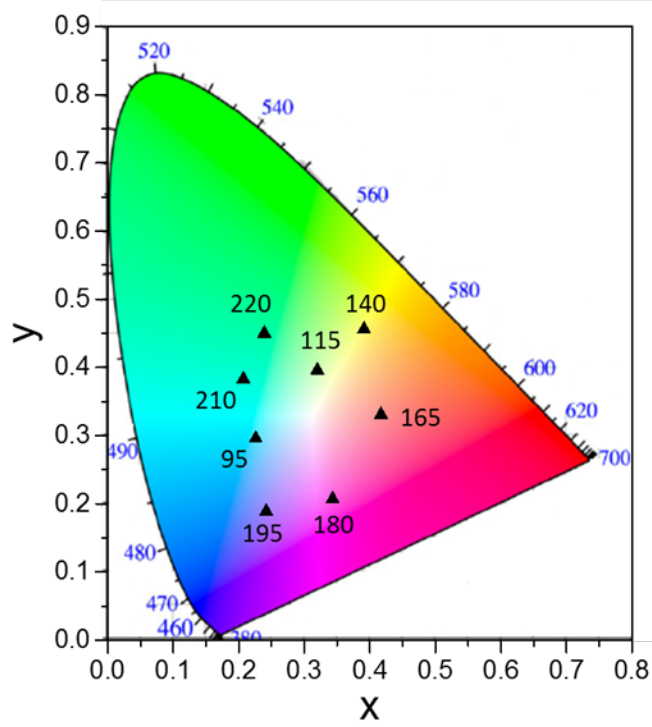
Figure S24: Colorful ST-PSCs color coordinates (x, y) the CIE 1931 chromaticity diagram. The PSCs' reflectance optical coordinates for ITO thickness varying from 95 to 220 nm have been reported in the CIE 1931 chromaticity diagram, showing the variety of the colors acheivable from the blue to red.

1. Bu, T., Liu, X., Zhou, Y., Yi, J., Huang, X., Luo, L., Xiao, J., Ku, Z., Peng, Y., Huang, F.*, et al.* (2017). A novel quadruple-cation absorber for universal hysteresis elimination for high efficiency and stable perovskite solar cells. Energy & Environmental Science *10*, 2509-2515.
2. Qiu, W., Merckx, T., Jaysankar, M., Masse de la Huerta, C., Rakocevic, L., Zhang, W., Paetzold, U.W., Gehlhaar, R., Froyen, L., Poortmans, J.*, et al.* (2016). Pinhole-free perovskite films for efficient solar modules. Energy & Environmental Science *9*, 484-489.
3. Yang, M., Li, Z., Reese, M.O., Reid, O.G., Kim, D.H., Siol, S., Klein, T.R., Yan, Y., Berry, J.J., van Hest, M.F.A.M.*, et al.* (2017). Perovskite ink with wide processing window for scalable high-efficiency solar cells. Nature Energy *2*, 17038.
4. Liao, H.-C., Guo, P., Hsu, C.-P., Lin, M., Wang, B., Zeng, L., Huang, W., Soe, C.M.M., Su, W.-F., Bedzyk, M.J.*, et al.* (2017). Enhanced Efficiency of Hot-Cast Large-Area Planar Perovskite Solar Cells/Modules Having Controlled Chloride Incorporation. Advanced Energy Materials *7*, 1601660.
5. Yeo, J.-S., Lee, C.-H., Jang, D., Lee, S., Jo, S.M., Joh, H.-I., and Kim, D.-Y. (2016). Reduced graphene oxide-assisted crystallization of perovskite via solution-process for efficient and stable planar solar cells with module-scales. Nano Energy *30*, 667-676.
6. Heo, J.H., Han, H.J., Kim, D., Ahn, T.K., and Im, S.H. (2015). Hysteresis-less inverted $CH_3NH_3PbI_3$ planar perovskite hybrid solar cells with 18.1% power conversion efficiency. Energy & Environmental Science *8*, 1602-1608.
7. Agresti, A., Pescetelli, S., Palma, A.L., Del Rio Castillo, A.E., Konios, D., Kakavelakis, G., Razza, S., Cinà, L., Kymakis, E., Bonaccorso, F.*, et al.* (2017). Graphene Interface Engineering for Perovskite Solar Modules: 12.6% Power Conversion Efficiency over 50 cm^2 Active Area. ACS Energy Letters *2*, 279-287.
8. Qiu, L., Liu, Z., Ono, L.K., Jiang, Y., Son, D.-Y., Hawash, Z., He, S., and Qi, Y. (2018). Scalable Fabrication of Stable High Efficiency Perovskite Solar Cells and Modules Utilizing Room Temperature Sputtered SnO_2 Electron Transport Layer. Advanced Functional Materials *0*, 1806779.
9. Chiang, C.-H., Nazeeruddin, M.K., Grätzel, M., and Wu, C.-G. (2017). The synergistic effect of H2O and DMF towards stable and 20% efficiency inverted perovskite solar cells. Energy & Environmental Science *10*, 808-817.
10. Chen, H., Ye, F., Tang, W., He, J., Yin, M., Wang, Y., Xie, F., Bi, E., Yang, X., Gratzel, M.*, et al.* (2017). A solvent- and vacuum-free route to large-area perovskite films for efficient solar modules. Nature.
11. Liu, Z., Qiu, L., Juarez-Perez, E.J., Hawash, Z., Kim, T., Jiang, Y., Wu, Z., Raga, S.R., Ono, L.K., Liu, S.*, et al.* (2018). Gas-solid reaction based over one-micrometer thick stable perovskite films for efficient solar cells and modules. Nature communications *9*, 3880.
12. Jiang, Y., Leyden, M.R., Qiu, L., Wang, S., Ono, L.K., Wu, Z., Juarez-Perez, E.J., and Qi, Y. (2018). Combination of Hybrid CVD and Cation Exchange for Upscaling Cs-Substituted Mixed Cation Perovskite Solar Cells with High Efficiency and Stability. Advanced Functional Materials *28*.
13. Leyden, M.R., Jiang, Y., and Qi, Y. (2016). Chemical vapor deposition grown formamidinium perovskite solar modules with high steady state power and thermal stability. Journal of Materials Chemistry A *4*, 13125-13132.
14. Grancini, G., Roldán-Carmona, C., Zimmermann, I., Mosconi, E., Lee, X., Martineau, D., Narbey, S., Oswald, F., De Angelis, F., Graetzel, M.*, et al.* (2017). One-Year stable perovskite solar cells by 2D/3D interface engineering. Nature communications *8*, 15684.
15. Di Giacomo, F., Shanmugam, S., Fledderus, H., Bruijnaers, B.J., Verhees, W.J.H., Dorenkamper, M.S., Veenstra, S.C., Qiu, W., Gehlhaar, R., Merckx, T.*, et al.* (2018). Up-scalable sheet-to-sheet production of high efficiency perovskite module and solar cells on 6-in. substrate using slot die coating. Solar Energy Materials and Solar Cells *181*, 53-59.
16. Deng, Y., Zheng, X., Bai, Y., Wang, Q., Zhao, J., and Huang, J. (2018). Surfactant-controlled ink drying enables high-speed deposition of perovskite films for efficient photovoltaic modules. Nature Energy.

17. Heo, J.H., Lee, M.H., Jang, M.H., and Im, S.H. (2016). Highly efficient CH3NH3PbI3−xClx mixed halide perovskite solar cells prepared by re-dissolution and crystal grain growth via spray coating. Journal of Materials Chemistry A *4*, 17636-17642.
18. Jung, E.H., Jeon, N.J., Park, E.Y., Moon, C.S., Shin, T.J., Yang, T.-Y., Noh, J.H., and Seo, J. (2019). Efficient, stable and scalable perovskite solar cells using poly(3-hexylthiophene). Nature *567*, 511-515.
19. Han, G.S., Kim, J., Bae, S., Han, S.-H., Kim, Y.J., Gong, O.Y., Lee, P., Ko, M.J., and Jung, H.S. (2019). Spin Coating Process for 10cm × 10cm Perovskite Solar Modules Enabled by Self-Assembly of SnO2 Nanocolloids. ACS Energy Letters.
20. Agresti, A., Pescetelli, S., Palma, A.L., Martin-Garcia, B., Najafi, L., Bellani, S., Moreels, I., Prato, M., Bonaccorso, F., and Di Carlo, A. (2019). Two-dimensional (2D) Material Interface Engineering for Efficient Perovskite Large-area Modules. ACS Energy Letters.
21. Bu, T., Li, J., Zheng, F., Chen, W., Wen, X., Ku, Z., Peng, Y., Zhong, J., Cheng, Y.-B., and Huang, F. (2018). Universal passivation strategy to slot-die printed SnO_2 for hysteresis-free efficient flexible perovskite solar module. Nature Communications *9*, 4609.
22. Yang, M., Kim, D.H., Klein, T.R., Li, Z., Reese, M.O., Tremolet de Villers, B.J., Berry, J.J., van Hest, M.F.A.M., and Zhu, K. (2018). Highly Efficient Perovskite Solar Modules by Scalable Fabrication and Interconnection Optimization. ACS Energy Letters *3*, 322-328.
23. Kim, J., Yun, J.S., Cho, Y., Lee, D.S., Wilkinson, B., Soufiani, A.M., Deng, X., Zheng, J., Shi, A., Lim, S.*, et al.* (2017). Overcoming the Challenges of Large-Area High-Efficiency Perovskite Solar Cells. ACS Energy Letters *2*, 1978-1984.
24. Jaysankar, M., Paetel, S., Ahlswede, E., Paetzold, U.W., Aernouts, T., Gehlhaar, R., and Poortmans, J. (2019). Toward scalable perovskite‐based multijunction solar modules. Progress in Photovoltaics: Research and Applications *0*.
25. Calabrò, E., Matteocci, F., Palma, A.L., Vesce, L., Taheri, B., Carlini, L., Pis, I., Nappini, S., Dagar, J., Battocchio, C.*, et al.* (2018). Low temperature, solution-processed perovskite solar cells and modules with an aperture area efficiency of 11%. Solar Energy Materials and Solar Cells *185*, 136-144.
26. Hu, Y., Si, S., Mei, A., Rong, Y., Liu, H., Li, X., and Han, H. (2017). Stable Large-Area ($10 \times 10 \, cm^2$) Printable Mesoscopic Perovskite Module Exceeding 10% Efficiency. Solar RRL *1*, 1600019.
27. Razza, S., Di Giacomo, F., Matteocci, F., Cinà, L., Palma, A.L., Casaluci, S., Cameron, P., D'Epifanio, A., Licoccia, S., Reale, A.*, et al.* (2015). Perovskite solar cells and large area modules (100 cm2) based on an air flow-assisted PbI_2 blade coating deposition process. Journal of Power Sources *277*, 286-291.
28. Troughton, J., Hooper, K., and Watson, T.M. (2017). Humidity resistant fabrication of $CH_3NH_3PbI_3$ perovskite solar cells and modules. Nano Energy *39*, 60-68.
29. Bu, T., Shi, S., Li, J., Liu, Y., Shi, J., Chen, L., Liu, X., Qiu, J., Ku, Z., Peng, Y.*, et al.* (2018). Low-Temperature Presynthesized Crystalline Tin Oxide for Efficient Flexible Perovskite Solar Cells and Modules. ACS applied materials & interfaces *10*, 14922-14929.
30. Priyadarshi, A., Haur, L.J., Murray, P., Fu, D., Kulkarni, S., Xing, G., Sum, T.C., Mathews, N., and Mhaisalkar, S.G. (2016). A large area (70 cm2) monolithic perovskite solar module with a high efficiency and stability. Energy & Environmental Science *9*, 3687-3692.
31. Cai, L., Liang, L., Wu, J., Ding, B., Gao, L., and Fan, B. (2017). Large area perovskite solar cell module. Journal of Semiconductors *38*, 014006.
32. Huang, Z., Hu, X., Liu, C., Meng, X., Huang, Z., Yang, J., Duan, X., Long, J., Zhao, Z., Tan, L.*, et al.* Water-Resistant and Flexible Perovskite Solar Cells via a Glued Interfacial Layer. Advanced Functional Materials *0*, 1902629.
33. Bu, T., Wu, L., Liu, X., Yang, X., Zhou, P., Yu, X., Qin, T., Shi, J., Wang, S., Li, S.*, et al.* (2017). Synergic Interface Optimization with Green Solvent Engineering in Mixed Perovskite Solar Cells. Advanced Energy Materials *7*, 1700576.

34. Deng, Y., Van Brackle, C.H., Dai, X., Zhao, J., Chen, B., and Huang, J. (2019). Tailoring solvent coordination for high-speed, room-temperature blading of perovskite photovoltaic films. Science advances *5*, eaax7537.
35. Jung, E.H., Jeon, N.J., Park, E.Y., Moon, C.S., Shin, T.J., Yang, T.-Y., Noh, J.H., and Seo, J. (2019). Efficient, stable and scalable perovskite solar cells using poly (3-hexylthiophene). Nature *567*, 511.